*minerals*

MDPI

*Article*

# Genesis of the Supergiant Shuangjianzishan Ag–Pb–Zn Deposit in the Southern Great Xing'an Range, NE China: Constraints from Geochronology, Isotope Geochemistry, and Fluid Inclusion

**Jiangpeng Shi [1,2], Guang Wu [1,2,3,*], Gongzheng Chen [3], Fei Yang [1,2], Tong Zhang [4], Biao Jiang [1] and Wenyuan Liu [5]**

[1] MNR Key Laboratory of Metallogeny and Mineral Assessment, Institute of Mineral Resources, Chinese Academy of Geological Sciences, Beijing 100037, China; shijiangpeng@stu.pku.edu.cn (J.S.); yangfeixt@126.com (F.Y.); jiangbiao334223@163.com (B.J.)
[2] School of Earth and Space Sciences, Peking University, Beijing 100871, China
[3] College of Earth Sciences, Hebei GEO University, Shijiazhuang 050031, China; a86793604@163.com
[4] Inner Mongolia Institute of Geological Survey, Hohhot 010020, China; zhangtnm@126.com
[5] The Provincial Key Laboratory of Mineral Resources, College of Zijin Mining, Fuzhou University, Fuzhou 350108, China; 15146@163.com
* Correspondence: wuguang65@163.com

**Abstract:** The supergiant Shuangjianzishan (SJS) Ag–Pb–Zn deposit, located in the southern Great Xing'an Range (SGXR), is the largest Ag deposit in China. The SJS deposit can be divided into two ore blocks: the Shuangjianzishan ore block and the Xinglongshan ore block. Given the importance of the Xinglongshan ore block in the SJS deposit, our work is focused on the Xinglongshan ore block. The vein orebodies in the Xionglongshan ore block mainly occur in the NW-, NNW-, and NNE-trending fault zones, and its mineralization is mainly related to a deep concealed syenogranite. Here, we present new geochronology, isotope geochemistry, and fluid inclusion data for the Xinglongshan ore block and provide additional insights into the metallogenic mechanism of the deposit. The dating results show that the syenogranite related to the mineralization formed at approximately 137 Ma, which is coherent with some previous age determinations in sulfides from the ore deposit. The mineralization of the Xinglongshan ore block can be divided into four stages: sphalerite–arsenopyrite–pyrite–chalcopyrite–quartz stage (stage I), sphalerite–galena–pyrite–silver-bearing mineral–quartz stage (stage II), sphalerite–galena–silver-bearing mineral–quartz–calcite stage (stage III), and weakly mineralized quartz–calcite stage (stage IV). Four types of fluid inclusions (FIs) have been identified within quartz and calcite veins: liquid-rich, gas-rich, pure-liquid, and pure-gas FIs. The homogenization temperatures in the four stages exhibit a gradual decrease, with stage I ranging from 253 to 302 °C, stage II from 203 to 268 °C, stage III from 184 to 222 °C, and stage IV from 153 to 198 °C, respectively. The salinity for stages I, II, III, and IV falls within the ranges of 3.4–6.6 wt% NaCl eqv., 2.6–7.2 wt% NaCl eqv., 2.9–7.0 wt% NaCl eqv., and 1.2–4.8 wt% NaCl eqv., respectively, indicative of a low-salinity ore-forming fluid. The $\delta^{18}O_{water}$ and δD values of the ore-forming fluid span from −13.9‰ to 7.4‰ and −145‰ to −65‰, with $\delta^{13}C_{V\text{-}PDB}$ values between −11.0‰ and −7.9‰. These values suggest that the ore-forming fluid predominantly originated from a mixture of magmatic and meteoric water. The $^{206}Pb/^{204}Pb$, $^{207}Pb/^{204}Pb$, and $^{208}Pb/^{204}Pb$ ratios of sulfides range from 18.278 to 18.361, 15.530 to 15.634, and 38.107 to 38.448, respectively. These ratios imply that the ore-forming material was primarily derived from the Early Cretaceous granitic magma, which resulted from the mixing of depleted mantle- and crustal-derived magmas. The fluid mixing was the dominant mechanism for mineral precipitation. The Xinglongshan ore block belongs to a magmatic-hydrothermal vein-type deposit related to the Early Cretaceous syenogranite, and the Shuangjianzishan ore block belongs to an intermediate sulfidation epithermal deposit related to coeval subvolcanic rocks. The Ag–Pb–Zn mineralization at Shuangjianzishan is genetically related to the Early Cretaceous volcanic–intrusive complex.



**Citation:** Shi, J.; Wu, G.; Chen, G.; Yang, F.; Zhang, T.; Jiang, B.; Liu, W. Genesis of the Supergiant Shuangjianzishan Ag–Pb–Zn Deposit in the Southern Great Xing'an Range, NE China: Constraints from Geochronology, Isotope Geochemistry, and Fluid Inclusion. *Minerals* **2024**, *14*, 60. https://doi.org/10.3390/min14010060

Academic Editor: Giorgio Garuti

Received: 21 October 2023
Revised: 28 December 2023
Accepted: 28 December 2023
Published: 3 January 2024

**Keywords:** zircon U–Pb age; fluid inclusion; H–O–C–Pb isotopes; volcanic–intrusive complex; Shuangjianzishan Ag–Pb–Zn deposit; southern Great Xing'an Range

## 1. Introduction

Silver (Ag), lead (Pb), and zinc (Zn) are widely developed in different genetic types of deposits [1–3]. The Ag–Pb–Zn deposits in the world can be divided into the following genetic types: (1) volcanic-hosted massive sulfide (VHMS or VMS) deposit [4–6]; (2) sedimentary exhalative (SEDEX) deposit [7–9]; (3) carbonate-hosted Mississippi Valley type (MVT) deposit [10]; (4) skarn-type deposit [11–13]; (5) magmatic-hydrothermal vein-type deposit [14,15]; and (6) epithermal deposit [16–18]. In addition, a few researchers have identified porphyry-type Ag–Pb–Zn deposits [19]. The vein-type Ag–Pb–Zn deposits occupy an important position in the global supply of Ag and base metals of Pb–Zn [18] and have become the hotspot of deposit research in the world. The southern Great Xing'an Range (SGXR), located in the eastern section of the Central Asian Orogenic Belt, spanning approximately 600 km in the northeast direction with a width of around 200 km [20–23], represents the preeminent Ag–Pb–Zn–Sn metallogenic belt in northern China. To date, forty-two Pb–Zn–Ag deposits have been discovered in the SGXR (Figure 1a,b), boasting proven reserves totaling 8,130,000 tons of Pb + Zn and 57,000 tons of Ag [21,24–26]. This area is distinguished by three types of Pb–Zn–Ag deposits: skarn type, subvolcanic-related vein type, and intrusion-related vein type (as depicted in Figure 1b). Some of these deposits also exhibit the presence of Cu and Sn, such as the Hua'aobaote deposit [26]. The ore-forming element assemblages of these deposits are mainly Ag–Pb–Zn, Ag–Pb–Zn–Cu, and Ag–Pb–Zn–Sn–Cu [21,27]. Recently, many studies have shown that the mineralization age of these deposits and the formation age of magmatic rocks related to mineralization are concentrated in the Late Jurassic to Early Cretaceous, suggesting that the mineralization is closely related to the late Yanshanian magmatic activity in the SGXR [22,28–32]. Among these Ag–Pb–Zn deposits in the SGXR, the Shuangjianzishan (SJS) deposit is the largest one, and it contains proven reserves of 15,214 tons Ag, 392,200 tons Pb, and 1,523,000 tons Zn, with average grades of 139.3 g/t Ag, 1.03% Pb, and 1.46% Zn, respectively, making this deposit the largest Ag deposit in China [18,33]. According to the classification criteria for the size of Zn–Pb–Ag deposits proposed by Large et al. [8,34], the SJS deposit belongs to a supergiant deposit.

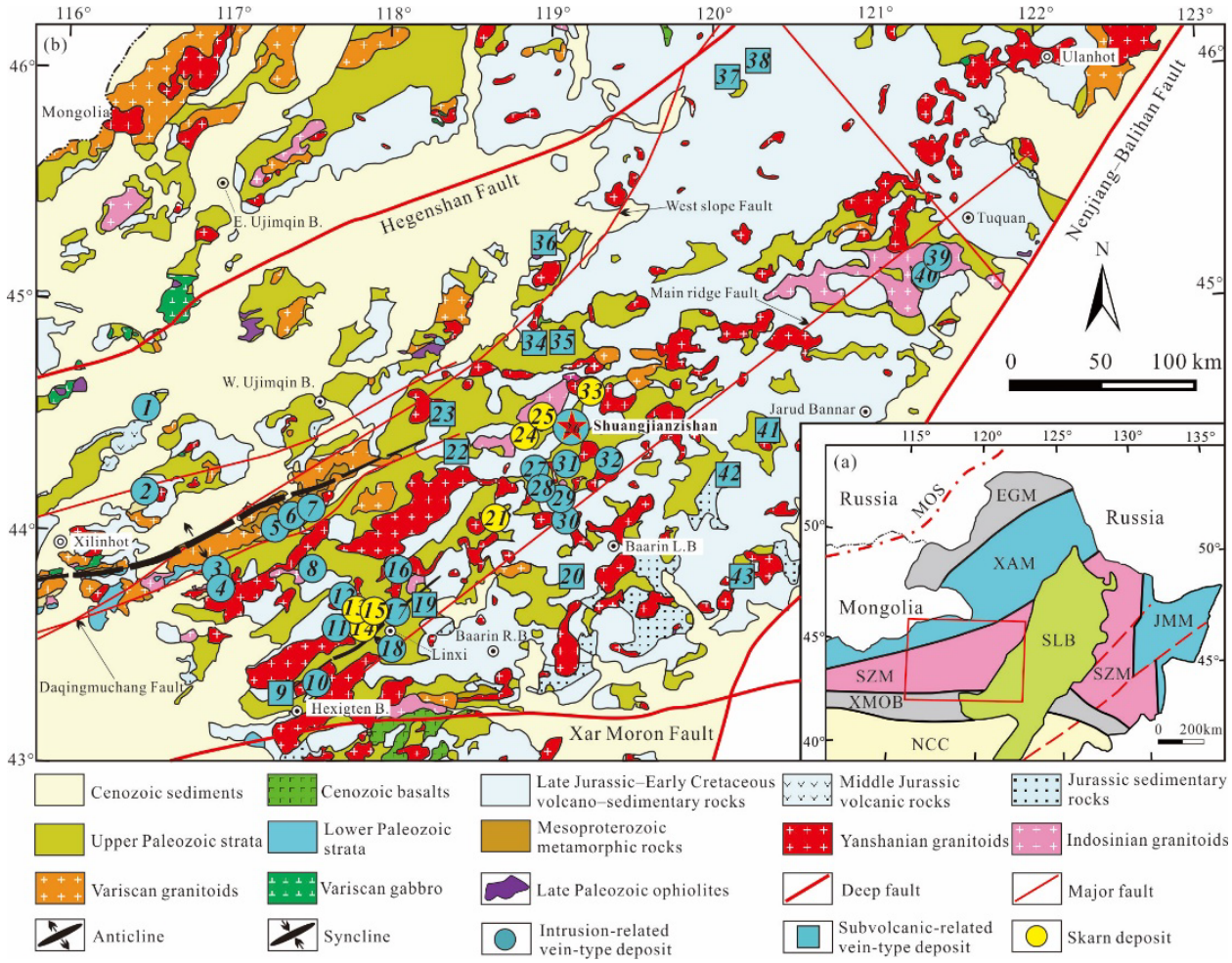


**Figure 1.** (**a**) Simplified geotectonic division of NE China (after [35]); (**b**) geological map of the southern Great Xing'an Range, highlighting the key Pb–Zn–Ag polymetallic deposit locations (modified after [27,36]). Notes: MOS = Mongol–Okhotsk suture zone; EGM = Ergun massif; SLB = Songliao basin; JMM = Jiamusi massif; SZM = Songnen–Zhangguangcai Range massif; NCC = North China craton; XMOB = Xar Moron orogenic belt; XAM = Xing'an massif. Detailed names of Pb–Zn–Ag–polymetallic deposits marked with numbers: 1 = Baiyinchagandongshan; 2 = Maodeng–Xiaogushan; 3 = Aobaoshan; 4 = Harchulutu; 5 = Bayanwula; 6 = Weilasituo; 7 = Bairendaba; 8 = Anle; 9 = Shidi; 10 = Dadi; 11 = Yonglong; 12 = Huangtuliang; 13 = Hadatu; 14 = Nasitai; 15 = Shalonggou; 16 = Xishijiangshan; 17 = Erbadi; 18 = Bianjiadayuan; 19 = Dajing; 20 = Hongguangmuchang; 21 = Daihuanggou; 22 = Chaowula; 23 = Wulanbaiqi; 24 = Baiyinnuoer; 25 = Nailinba; 26 = Shuangjianzishan; 27 = Aguihundelun; 28 = Baiyinwula; 29 = Biliutaibei; 30 = Taipingdi; 31 = Erdaoyingzi; 32 = Dongshan; 33 = Haobugao; 34 = Bujinhei; 35 = Shabulengshan; 36 = Huaaobaote; 37 = Zhamuqin; 38 = Fuxingtun; 39 = Meng'entaolegai; 40 = Maohuduger; 41 = Shuiquan; 42 = Aobaotu; 43 = Panjiaduan.

Previous researchers have extensively investigated the SJS deposit, covering a range of aspects such as the geological characteristics of the deposit [33], geochronology and petrogeochemistry of ore-forming rocks [18,37,38], mineralogical assemblages [39], and the origins of ore-forming fluids and materials [18,40]. Nonetheless, the mineralization age and the ore genesis of the SJS deposit still remain controversial. The mineralization age of the SJS deposit, as investigated by previous researchers, falls within a wide range of 160–130 Ma [18,24,27,33,37,39,40]. Furthermore, there is an ongoing debate regarding the types of mineralization in the SJS deposit, which primarily revolves around two main types: the epithermal type [18,37] and the magmatic-hydrothermal vein type [27,33]. Further study is needed on the origin and evolution of ore-forming fluids, source of ore-forming

materials, mechanisms of metal precipitation, and genetic types of the SJS deposit. In this study, we present new data concerning the zircon U–Pb age, fluid inclusions, and H–O–C–Pb isotopes associated with the SJS deposit. These various data are used to decipher the source, feature, and evolution of the ore-forming fluid and to explore the metallogenic mechanism. As a result, we are able to constrain the genesis of the SJS Ag–Pb–Zn deposit.

## 2. Regional Geology

The SGXR is located in the central section of the Songnen–Zhangguangcai Range block (SZM, Figure 1a), and four boundaries of the east, west, north, and south are the Nenjiang–Balihan fault, East Ujimqin Banner–Xilinhot belt, Hegenshan fault, and Xar Moron fault, respectively. The SGXR underwent sequential tectonic control from the Paleo-Asian Ocean in the Paleozoic, followed by the Mongol–Okhotsk Ocean and Paleo-Pacific tectonic domains in the Mesozoic [27,41,42]. These tectonic transitions are documented as intricate geodynamic processes marked by multiple tectonic events. The geological formations visible in the SGXR comprise the Mesoproterozoic metamorphic rock series, Paleozoic marine volcanic–clastic rocks, Paleozoic continental clastic rocks, Mesozoic continental volcanic–clastic rocks, as well as Cenozoic basalt, and Quaternary loose sediment (Figure 1b). Prominent geological structures within the SGXR encompass the Ganzhuermiao anticline, Linxi syncline, Hegenshan fault, and Xar Moron fault, which originated during the Late Paleozoic [43,44], and the Nenjiang–Balihan fault formed during the Mesozoic [45,46], which constitute the basic tectonic framework of the SGXR. This region underwent widespread Variscan, Indosinian, and Yashanian volcanic and intrusive activity, and different types of granitoids emplaced at different stages are widely distributed. Most importantly, the Mesozoic I- and A-type granitoids comprise > 20% of the surface area in the SGXR [14], which was triggered by the subduction of the Paleo-Pacific plate, making the eastern Asian Mesozoic continental margin the most important metallogenic area [18]. Numerous studies showed that the Jurassic subduction of the Paleo-Pacific plate led to the extension of the back-arc area and the lithospheric delamination and that the subsequent rollback of the subduction plate triggered the large-scale emplacement of the Early Cretaceous volcanic–intrusive complex [47,48].

The SGXR hosts a number of intrusion-related vein types, subvolcanic-related vein types, and skarn-type polymetallic (Ag–Pb–Zn–Cu–Sn) deposits [18,22,27]. Regional mineralization is spatially and temporally closely related to the Jurassic to Cretaceous volcanic–intrusive complex [40]. These deposits are predominantly distributed along an approximately 600-km-long and 200-km-wide zone of NE-trending and are mainly hosted by the Permian strata and Mesozoic granites. With the discoveries of a large number of new Ag–Pb–Zn deposits recently [28,49], the Ag–Pb–Zn–Sn–Cu metallogenic belt of the SGXR has become more important.

## 3. Ore District and Deposit Geology

### *3.1. Ore District Geology*

The supergiant SJS Ag–Pb–Zn deposit (44°29′30″–44°31′30″ N, 119°03′30″–119°10′00″ E) is located in the north of Baarin Left Banner, Chifeng City, Inner Mongolia Autonomous Region, which is tectonically located in the central part of the Songnen–Zhangguangcai Range massif (Figure 1a). The exposed lithological units in the SJS ore district can be seen in Figure 2.

The Permian strata, including the Shoushangou, Dashizhai, Zhesi, and Linxi formations, are mainly composed of marine clastic rocks and intermediate–felsic volcanic rocks, with a small amount of continental calstic rocks. The ore bodies of the SJS deposit are mainly hosted in the Dashizhai Formation, which is predominantly characterized by marine thick sandstone layers, along with andesite, silty slate, altered andesite, basalt, and andesitic tuff, with a total thickness exceeding 900 m. The Mesozoic strata, including the Xinmin, Manketouebo, Manitu, and Baiyin'gaolao formations, are mainly composed of continental intermediate–felsic volcanic rocks and pyroclastic rocks with a small amount of calstic rocks. The Yanshanian granites are exposed 2 km northwest of the SJS deposit and

lie concealed in the central part of the ore district. The concealed granite bodies revealed by deep drilling include biotite granite, syenogranite, and granite. In addition, granite porphyry, diorite porphyry, and rhyolite porphyry occur as NW- or NE-trending veins, dipping SW at ~60° and typically measuring up to 300 m long and 8 m wide, some of which are crosscut by Ag–Pb–Zn mineralized veins. The main structures in the ore district include the NE-trending Yaoerya–Pangjiawan anticline, NW-trending fracture zone, and NNE- and NW-trending faults.

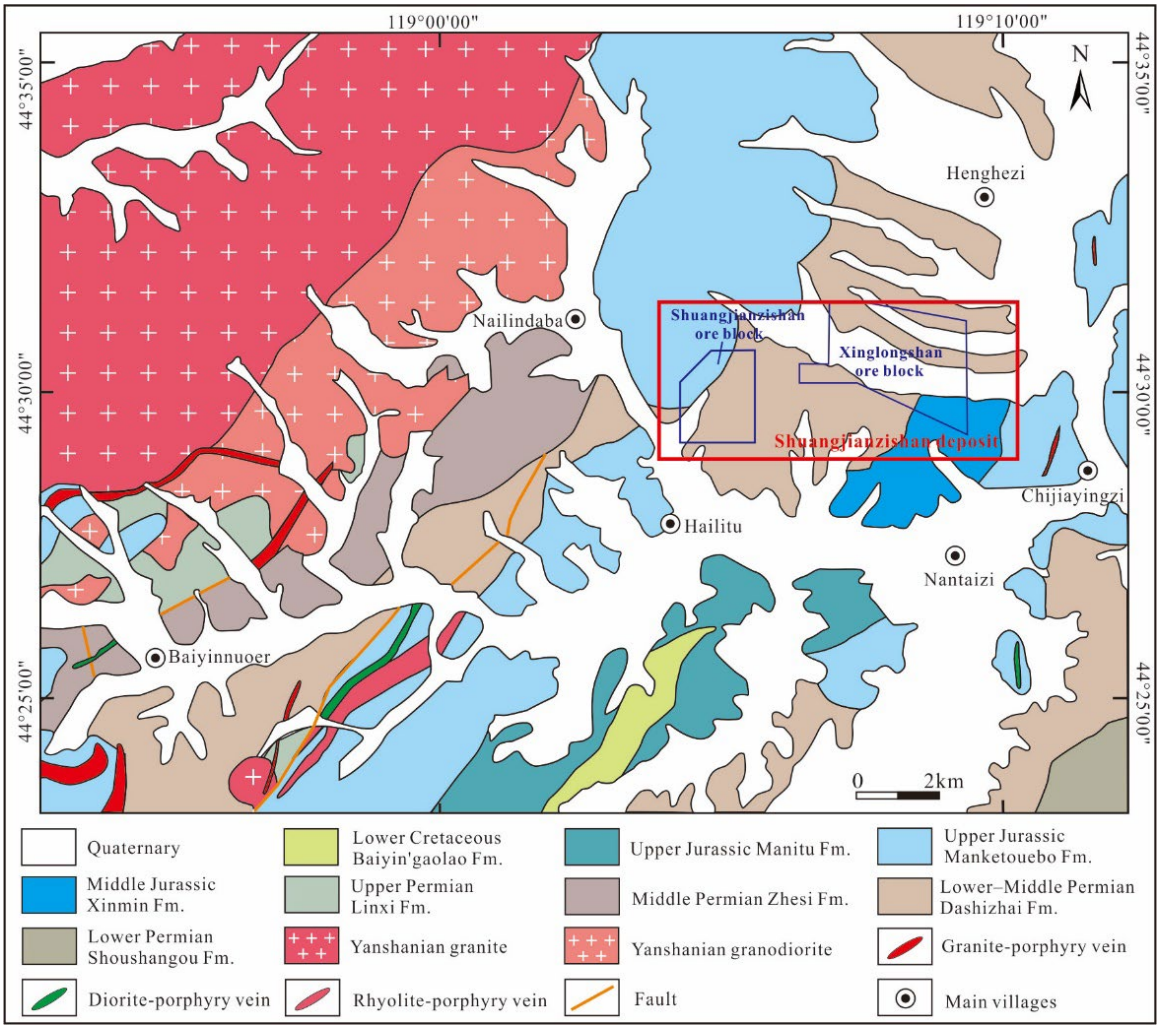


**Figure 2.** Simplified regional geological map of the Shuangjianzishan area (modified after [25,33]).

### *3.2. Ore Deposit Geology*

The SJS Ag–Pb–Zn deposit was discovered in 2013 and was divided into two ore blocks, namely the western ore block (Shuangjianzishan ore block) and the eastern ore block (Xinglongshan ore block) [18] (Figure 2). The Xinglongshan ore block accounts for the vast majority of the total reserves of the SJS deposit [18,33]. A total of 276 industrial orebodies have been delineated in the block, including 39 large-sized, 32 medium-sized, and 205 small-sized orebodies [18,33]. However, only 4 industrial orebodies, including 1 medium-sized and 3 small-sized orebodies, have been delineated in the Shuangjianzishan ore block [18,33].

#### 3.2.1. Xinglongshan Ore Block

The exposed strata in the Xinglongshan ore block include the Lower–Middle Permian Dashizhai Formation, Middle Jurassic Xinmin Formation, and Upper Jurassic Manketouebo

Formation (Figure 3a). Except for a small amount of rhyolite porphyry veins exposed on the surface, other granitic intrusions, including granite, biotite granite, and syenogranite, are all concealed below 500 m of the ore block surface (Figure 3a,c). The fault structures, including NE-, NW-, and NEE-trending faults, are well-developed (Figure 3a). According to the direction of orebodies, the orebodies in the Xinglongshan ore block are mainly divided into (1) NW-trending Ag–Pb–Zn (Cu) ore vein group, (2) NNW-trending Ag–Pb–Zn orebodies, and (3) NNE-trending Ag–Pb–Zn orebodies. In addition, small amounts of near E–W-trending Au-bearing Ag–Pb–Zn orebodies are also developed in this ore block.

(1) The NW-trending Ag–Pb–Zn (Cu) ore vein group: The orebodies in the ore vein group distributed in the central and eastern parts of the ore block are controlled by a NW-trending thick and large fractured zone. The ore-hosting rocks are slate and silty slate of the Lower–Middle Permian Dashizhai Formation (Figure 3b). The overall strike of the ore-vein group is 300°–310°, inclined towards the southwest, with dip angles of 50°–65° and a length > 2000 m and a width > 1200 m. The ore-vein group is mainly composed of Ag–Pb–Zn orebodies and Ag–Zn orebodies, with a small amount of Zn orebodies and Ag–Cu–Pb–Zn orebodies (Figure 3b). The individual orebodies occur as veins, usually having a length of 100–800 m and a thickness of 1–10 m, with a maximum thickness exceeding 100 m (Figure 3b). The ore structure is mainly of fine-vein, stockwork, disseminated, and dense disseminated (Figure 4a–d). The major wall-rock alteration includes silicification and chloritization, with minor sericitization (Figure 4a–d). These altered minerals mainly occur in the form of fine veins and stockworks within a thick NW-trending alteration zone, with minor veins and crumbs of quartz. The grade of the Ag–Pb–Zn orebodies is relatively low, with average grades of 98 g/t Ag, 1.6% Zn, and 0.6% Pb, respectively [23]. The Ag–Cu–Pb–Zn orebodies usually occur at the top of the ore-vein group, with a controlled length greater than 300 m and a thickness of 0.6–2.8 m. The Ag–Cu–Pb–Zn orebodies have average grades of 263 g/t Ag, 0.7% Cu, 2.2% Zn, and 0.9% Pb, respectively [23].
(2) The NNW-trending Ag–Pb–Zn orebodies: These orebodies, mainly distributed in the central and eastern parts of the ore block, are controlled by NNW-trending faults. The overall trend of these orebodies is approximately 310°, with a thickness of 3–15 m and a length of > 400 m. The ore structure is mainly of massive and vein (Figure 4e,f). The wall-rock alteration is characterized by silicification and carbonation, with minor chloritization, and quartz and calcite mainly occur as fine veins within the orebodies and within a range of no more than two meters nearby (Figure 4e,f). The NW-trending Ag–Pb–Zn orebodies have average grades of 400 g/t Ag (some up to 10,000 g/t), 2.8% Zn, and 4.3% Pb, respectively [23].
(3) The NNE-trending Ag–Pb–Zn orebodies: These orebodies, distributed in the eastern part of the ore block, are composed of five parallel orebodies. They are controlled by NNE-trending faults, which dip to NWW at > 65°. The ore structure is mainly of massive and vein (Figure 4g,h). The types and distribution characteristics of wall-rock alteration are similar to those of the NNW-trending orebodies. These orebodies have a thickness of 2–6 m and a control length > 600 m, with average grades of 400 g/t Ag, 2.5% Zn, and 3.2% Pb, respectively [23].

The near E–W-trending Au-bearing Ag–Pb–Zn orebodies occur as veins and are interspersed within the aforementioned NW-, NNW-, and NNE-trending Ag–Pb–Zn orebodies. The ore structure is mainly of fine veins and disseminated (Figure 4i). The wall-rock alteration is characterized by silicification and carbonation, which develop in the form of clumps and veins within the orebodies and nearby wall-rocks (Figure 4i).

#### 3.2.2. Shuangjianzishan Ore Block

The exposed strata in the Shuangjianzishan ore block include the Lower–Middle Permian Dashizhai Formation and Upper Jurassic Manketouebo Formation (Figure 2). The ore block is located within a Yanshanian volcanic edifice, and no intrusives are exposed. The orebodies are controlled by two sets of NW- and NE-trending faults, which belong

to the derived structures of the volcanic edifice. The NW-trending faults dip to NE at approximately 50°, and NE-trending faults dip to SE at 57°–61°. The NW-trending #501 orebody is the largest in the Shuangjianzishan ore block. Its ore-hosting rocks consist of andesitic tuff, breccia tuff, altered andesite, and argillaceous slate. The orebody is 332 m long, with an inclined depth of 240 m and a thickness of 4.88 m. Its average grades are 99 g/t Ag, 1.0% Pb, and 0.8% Zn, respectively.

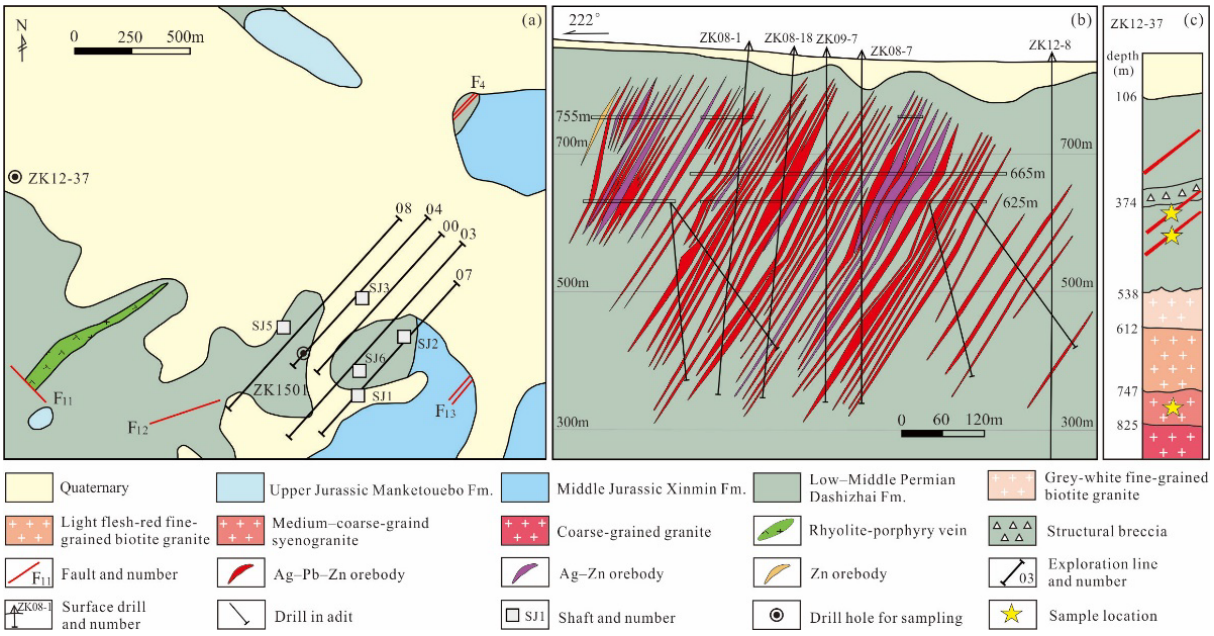


**Figure 3.** (**a**) Geologic map of the Xinglongshan ore block (modified after [39]); (**b**) simplified geological section along the 00-exploration line, showing the occurrence of the NW-trending Ag–Pb–Zn (Cu) ore vein group (modified after [39]); (**c**) log of drill no. ZK12-37, showing the distribution of granites (modified after [18]).

### 3.2.3. Ore Mineralogy and Textures of the Xinglongshan Ore Block

The ore minerals in the NW-trending ore vein group are mainly sphalerite, arsenopyrite, and pyrite, followed by galena, chalcopyrite, and pyrrhotite, with minor canfieldite and cassiterite (Figure 5a–d). The major gangue minerals are quartz, followed by chlorite, with minor sericite (Figure 5m,p). The ore texture includes anhedral granular, subhedral granular, euhedral granular, metasomatic dissolution, poikilitic, and exsolution textures (Figure 5a–d). Sphalerite is chiefly of anhedral granular texture (Figure 5a–c) and occasionally involves cassiterite particles, developing a poikilitic texture (Figure 5d); arsenopyrite is mainly of subhedral–euhedral granular texture (Figure 5c), with minor anhedral granular texture (Figure 5a); pyrite is mainly of anhedral granular texture, followed by subhedral–euhedral granular texture (Figure 5b); galena, pyrrhotite, canfieldite, and cassiterite are chiefly of anhedral granular texture (Figure 5a,c,d); chalcopyrite occurs as emulsion droplet within sphalerite, developing an exsolution texture (Figure 5a,b), and chalcopyrite is generally replaced by galena and canfieldite, developing a metasomatic dissolution texture (Figure 5c).

The ore minerals in the NNW-trending orebodies are mainly sphalerite and galena, followed by freibergite, polybasite, pyrargyrite, and aguilarite, with minor canfieldite, chalcopyrite, and argentite (Figure 5e–h). The major gangue minerals are mainly quartz and chlorite (Figure 5n,p). The ore texture includes anhedral granular, metasomatic dissolution, and exsolution textures (Figure 5e–h). Chalcopyrite occurs as an emulsion droplet within sphalerite, developing an exsolution texture (Figure 5e,f); galena is often replaced by freibergite and polybasite (Figure 5e), chalcopyrite and pyrargyrite (Figure 5f), and canfieldite and aguilarite (Figure 5g), developing a metasomatic dissolution texture.


**Figure 4.** Representative photos of orebodies in the Xinglongshan ore block. (**a**) fine-vein Ag–Pb–Zn orebody of the NW-trending ore vein group; (**b**) stockwork Pb–Zn orebody of the NW-trending ore vein group orebody; (**c**) disseminated Pb–Zn ore of the NW-trending ore vein group, with silification; (**d**) dense disseminated Cu–polymetallic ore of the NW-trending ore vein group, with silification; (**e**) high-grade Ag–Pb–Zn orebody of the NNW-trending orebodies, with silification; (**f**) Ag–Pb–Zn orebody of the NNW-trending orebodies, with silification and carbonation; (**g**) high-grade Ag–Pb–Zn orebody of the NNE-trending orebodies; (**h**) high-grade Ag–Pb–Zn orebody of the NNE-trending orebodies, with silification and carbonation; (**i**) Au-bearing Ag–Pb–Zn orebody with silification and carbonation, occurring in the near E–W-trending faults. Abbreviations: Cal = calcite; Ccp = chalcopyrite; Gn = galena; Kut = kustelite; Qtz = quartz; Sp = sphalerite.

The ore minerals in the NNE-trending orebodies are mainly sphalerite and galena, followed by pyrite, freibergite, polybasite, pyrargyrite, canfieldite, and argentite (Figure 5i–k). The gangue minerals are mainly quartz and calcite (Figure 5o,p), with minor chlorite. The ore texture includes anhedral granular, metasomatic dissolution, poikilitic, and exsolution textures (Figure 5i–k). Canfieldite replaces galena along the edge of galena, developing a metasomatic dissolution texture (Figure 5i); chalcopyrite occurs as an emulsion droplet within sphalerite, developing an exsolution texture (Figure 5j); sphalerite involves cassiterite and galena, developing a poikilitic texture, and canfieldite replaces galena and sphalerite, developing a metasomatic dissolution texture (Figure 5k).

The ore minerals in the near E–W-trending Au-bearing Ag–Pb–Zn orebodies are mainly sphalerite, galena, pyrite, pyrargyrite, freibergite, argentite, and polybasite, with minor native silver and kustelite (Figure 5l). The gangue minerals are mainly quartz and calcite (Figure 5p). The ore texture includes anhedral granular and metasomatic dissolution textures (Figure 5l).

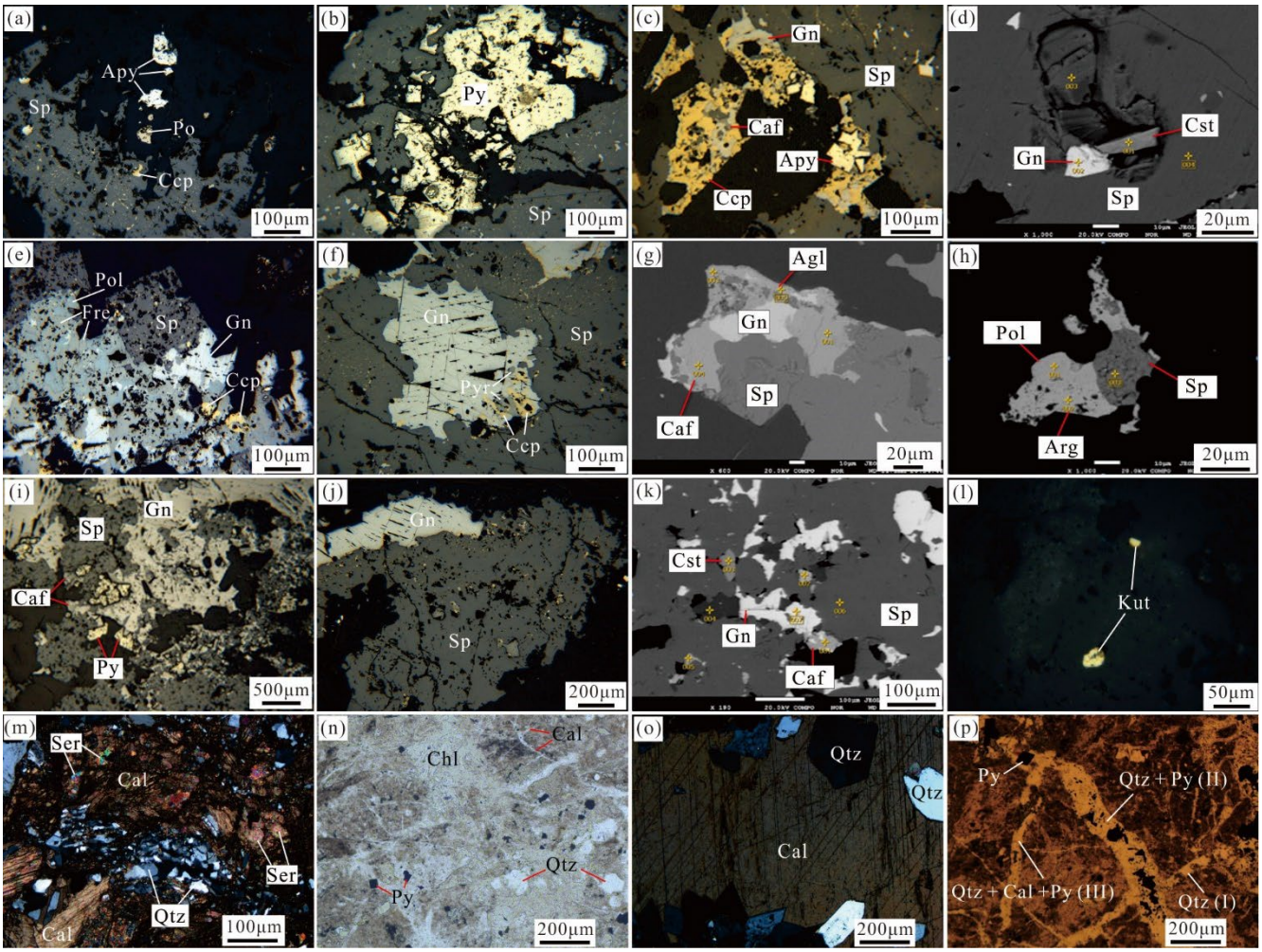


**Figure 5.** Representative photos of ores and major wall-rock alteration types in the Xinglongshan ore block. (**a**–**d**) Mineral assemblages of the NW-trending ore vein group, including sphalerite, arsenopyrite, pyrite, chalcopyrite, galena, pyrrhotite, canfieldite, and cassiterite; (**e**–**h**) mineral assemblages of the NNW-trending orebodies, including sphalerite, galena, freibergite, polybasite, pyrargyrite, aguilarite, canfieldite, chalcopyrite, and argentite; (**i**–**k**) mineral assemblages of the NNE-trending orebodies, including sphalerite, galena, pyrite, freibergite, polybasite, pyrargyrite, canfieldite, and argentite; (**l**) kustelite occurring within quartz and/or freibergite in the near E–W-trending Au-bearing Ag–Pb–Zn orebodies; (**m**) sericitization and silicification in stage I, superimposed by later carbonation; (**n**) silicification and chloritization developing in stages II and III, superimposed by later carbonation; (**o**) silicification and carbonation developing in stage III; (**p**) vein bodies cutting relationship, displaying quartz vein of stage I, quartz–pyrite vein of stage II, and quartz–calcite–pyrite vein of stage III. (**a**–**c**,**e**,**f**,**i**,**j**,**l**): plainlight under reflected light; (**d**,**g**,**h**,**k**): back-scatter electron (BSE) images; (**m**) and (**o**): cross-polarized light under transmitted light; (**n**) and (**p**): plainlight under transmitted light. Abbreviations: Agl = aguilarite; Apy = arsenopyrite; Arg = argentite; Caf = canfieldite; Cal = calcite; Ccp = chalcopyrite; Chl = chlorite; Cst = cassiterite; Fre = freibergite; Gn = galena; Kut = kustelite; Po = pyrrhotite; Pol = polybasite; Py = pyrite; Pyr = pyrargyrite; Qtz = quartz; Ser = sericite; Sp = sphalerite.

### 3.2.4. Mineralization Stages

Based on mineral assemblages, ore fabrics, and crosscutting relationships between the veins, the ore-forming process in the Xinglongshan ore block can be divided into four stages (Figure 6): (1) sphalerite–arsenopyrite–pyrite–chalcopyrite–quartz stage (stage I); (2) sphalerite–galena–pyrite–silver-bearing minerals–quartz stage (stage II); (3) sphalerite–

galena–silver-bearing minerals–quartz–calcite stage (stage III); and (4) weakly mineralized quartz–calcite stage (stage IV). The ore minerals of stage I are mainly iron sphalerite, arsenopyrite, and pyrite, followed by chalcopyrite, galena, pyrrhotite, and aguilarite, with minor canfieldite, freibergite, polybasite, and cassiterite. The ore minerals of stage II are mainly sphalerite and galena, followed by pyrite, aguilarite, canfieldite, freibergite, polybasite, and pyrargyrite, with minor pyrrhotite, arsenopyrite, and chalcopyrite. The ore minerals of stage III are mainly sphalerite and galena, followed by pyrite, canfieldite, freibergite, polybasite, pyrargyrite, and argentite. In addition, kustelite and native silver can be observed within Au-bearing Ag–Pb–Zn ores of stage III. The ore minerals of stage IV are dominated by pyrite, with minor sphalerite, galena, argentite, and native silver.

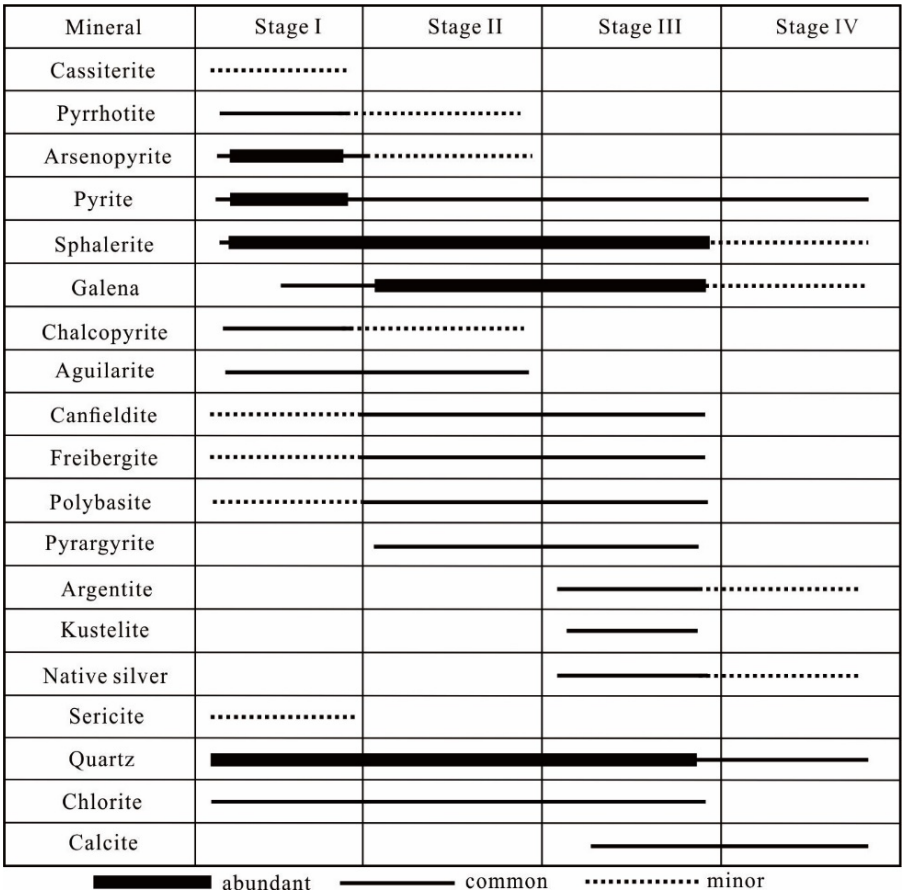


**Figure 6.** The paragenetic sequence of minerals in the Xinglongshan ore block.

## 4. Sampling and Analytical Methods

### *4.1. Sampling*

In this research, we carefully handpicked 37 samples sourced from diverse mining levels and drill holes in the Xinglongshan ore block. These samples were chosen to undergo a range of analytical processes, including U-Pb dating, fluid inclusion analysis, and H–O–C–Pb isotope investigations.

These samples, mainly medium-coarse-grained syenogranite specimens, characterized by their predominant composition of K-feldspar (50%), quartz (35%), plagioclase (10%), and biotite (5%), were carefully selected for laser ablation inductively coupled plasma mass spectrometry (LA-ICP-MS) zircon U-Pb dating, as indicated in Table 1 (refer to Figures 3c and 7). For fluid inclusion (FI) analysis, we collected six quartz samples and two calcite samples, each sourced from four distinct mineralization stages, as outlined in Table 1. In addition, thirteen quartz samples obtained from these mineralization stages underwent H–O isotope analysis, while seven calcite samples, specifically from stages III and IV, were

subjected to H–O–C isotope analysis. Detailed information about these samples can be found in Table 1. Furthermore, our investigation extended to the analysis of twenty sulfide samples derived from seven different samples across the four mineralization stages. This set of samples encompassed seven galena, seven sphalerite, and six pyrite specimens. A comprehensive overview of these samples can be found in Table 1, alluding to the extensive and thorough nature of our analytical approach.

**Table 1.** List of analytical samples for the Xinglongshan ore block.

| Sample | Orebody No./Lithology | Position | Stage | Mineral | Analysis |
|---|---|---|---|---|---|
| SJ49-1 | Syenogranite | Drill No. ZK12-37 at 780 m deep | | Zrn | U–Pb dating |
| SJ49-10 | Syenogranite | Drill No. ZK12-37 at 1071 m deep | | Zrn | U–Pb dating |
| SJ14 | No. 2 Pb–Zn–Cu orebody | 625-m level | I | Qtz | FIs study |
| SJ6 | Disseminated Pb–Zn–Ag orebody | 625-m level | II | Qtz | FIs study |
| SJ31 | No. 2 Pb–Zn–Ag orebody | Drill No. ZK1501 at 1207 m deep | II | Qtz | FIs study |
| SJ11 | No. 1-3 Pb–Zn–Ag orebody | 625-m level | III | Qtz | FIs study |
| SJ12 | No. 2 Pb–Zn–Ag orebody | 625-m level | III | Qtz | FIs study |
| SJ13-1 | Pb–Zn–Ag–Au orebody | 625-m level | III | Cal | FIs study |
| SJ8 | No. 2 Pb–Zn–Ag mineralized orebody | 625-m level | IV | Qtz | FIs study |
| SJ45 | No. 2-16 Pb–Zn–Ag mineralized body | 665-m level | IV | Cal | FIs study |
| 2-3m-3 | No. 2-3 Pb–Zn–Cu orebody | 625-m level | I | Qtz | H–O isotopes |
| 8-16m-1 | No. 8-16 Pb–Zn–Cu orebody | 665-m level | I | Qtz | H–O isotopes |
| 1m-3 | No. 1 Pb–Zn–Cu orebody | 625-m level | I | Qtz | H–O isotopes |
| 8-16m-3 | No. 8-16 Pb–Zn–Cu orebody | 665-m level | I | Qtz | H–O isotopes |
| 8-16m-4 | No. 8-16 Pb–Zn–Cu orebody | 665-m level | I | Qtz | H–O isotopes |
| 2-3m-7 | No. 2-3 Pb–Zn–Cu orebody | 625-m level | I | Qtz | H–O isotopes |
| 2-3m-6 | No. 2-3 Pb–Zn–Ag orebody | 625-m level | II | Qtz | H–O isotopes |
| 1-5-1m-2 | No. 1-5-1 Pb–Zn–Ag–Au orebody | 625-m level | II | Qtz | H–O isotopes |
| 5#KD-2-1 | No. 2 Pb–Zn–Ag orebody | 625-m level | II | Qtz | H–O isotopes |
| 5#KD-2-2 | No. 2 Pb–Zn–Ag orebody | 625-m level | II | Qtz | H–O isotopes |
| ZD4-1-1m-1 | No. 1-1 Pb–Zn–Ag orebody | 665-m level | III | Cal | H–O–C isotopes |
| ZD4-1-1m-2 | No. 1-1 Pb–Zn–Ag orebody | 665-m level | III | Cal | H–O–C isotopes |
| ZD4-1-1m-3 | No. 1-1 Pb–Zn–Ag orebody | 665-m level | III | Cal | H–O–C isotopes |
| ZD4-1-1m-4 | No. 1-1 Pb–Zn–Ag orebody | 665-m level | III | Qtz | H–O isotopes |
| ZD4-1-1m-4 | No. 1-1 Pb–Zn–Ag orebody | 665-m level | III | Cal | H–O–C isotopes |
| 5#KD-1 | No. 1-1 Pb–Zn–Ag mineralized body | 665-m level | IV | Qtz | H–O isotopes |
| 8-12m-1 | No. 8-12 Pb–Zn–Ag mineralized body | 665-m level | IV | Cal | H–O–C isotopes |
| 8-12m-2 | No. 8-12 Pb–Zn–Ag mineralized body | 665-m level | IV | Qtz | H–O isotopes |
| 8-12m-2 | No. 8-12 Pb–Zn–Ag mineralized body | 665-m level | IV | Cal | H–O–C isotopes |
| 8-12m-3 | No. 8-12 Pb–Zn–Ag mineralized body | 665-m level | IV | Cal | H–O–C isotopes |
| 2-3m-1 | No. 2-3 Pb–Zn–Cu orebody | 625-m level | I | Gn, Sp, Py | Pb isotope |
| 2m-3 | No. 2-3 Pb–Zn–Cu orebody | 625-m level | I | Gn, Sp, Py | Pb isotope |
| 1m-1 | No. 1 Pb–Zn–Cu orebody | 625-m level | I | Gn, Sp, Py | Pb isotope |
| ZD5-1-1m-1 | No. 1-1 Pb–Zn–Ag orebody | 625-m level | II | Gn, Sp | Pb isotope |
| ZD4-1-1m-1 | No. 1-1 Pb–Zn–Ag orebody | 665-m level | III | Gn, Sp, Py | Pb isotope |
| 8-16m-2 | No. 8-16 Pb–Zn–Ag mineralized body | 665-m level | IV | Gn, Sp, Py | Pb isotope |
| 8-12m-1 | No. 8-12 Pb–Zn–Ag mineralized body | 665-m level | IV | Gn, Sp, Py | Pb isotope |

Abbreviations: Cal = calcite; Gn = Galena; Py = pyrite; Qtz = quartz; Sp = sphalerite; Zrn = zircon.

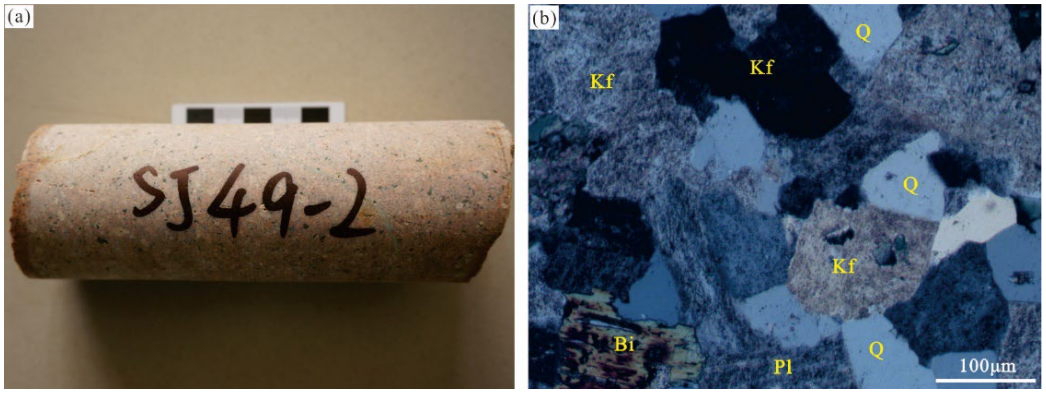


**Figure 7.** Field (**a**) and microscopic (**b**) photos of concealed syenogranite in the Xinglongshan ore block.

### *4.2. Syenogranite Zircon U–Pb Dating*

Zircon grains were separated through traditional heavy liquid and magnetic separation techniques. Following this, they underwent meticulous purification through handpicking under a binocular microscope, a process carried out at the Langfang Chengxin Geological Service Co., Ltd. in Hebei Province, China. The handpicked zircon grains were mounted in epoxy and polished to expose the cores of the grains for subsequent cathodoluminescence (CL) imaging and zircon U–Pb analyses. The CL images were obtained at the Zircon Navigation Technology Co., Ltd., Beijing, China. The LA-ICP-MS zircon U–Pb dating was undertaken at the Yandu Zhongshi Testing Technology Co., Ltd., Beijing, China, using a Finnigan Neptune MC-ICP-MS attached to a New Wave UP 213 laser ablation system with an in-house sample cell. The detailed analytical procedures were similar to those described by Griffin et al. [50] and Hou et al. [51]. U–Pb fractionation was corrected using zircon standard GEMOC GJ-1 ($^{207}Pb/^{206}Pb$ age of 608.5 ± 1.5 Ma, [52]), and accuracy was controlled using zircon standard Mud Tank (intercept age of 732 ± 5 Ma, [53]). U–Pb ages were calculated from raw signal data using ISOPLOT 3.0 [54]. Because $^{204}Pb$ could not be measured due to a low signal and interference from $^{204}Hg$ in the gas supply, a common lead correction was carried out using the EXCEL program ComPbCorr#3.15G [55]. Errors on individual analyses by LA-ICP-MS were quoted at the 1σ level, while errors on pooled ages were quoted at the 95% (2σ) confidence level.

### *4.3. Fluid Inclusion Microthermometry and Laser Raman Spectroscopy*

Microthermometric measurements of fluid inclusions (FIs) were conducted at the Institute of Mineral Resources, Chinese Academy of Geological Sciences, located in Beijing, China. This process utilized a LINKAM THMSG 600 programmable heating-freezing stage paired with a high-quality German Zeiss microscope. The homogenization temperature spanned from −190 °C to 600 °C, with estimated accuracies of ±0.1 °C between −100 °C and 25 °C, ±1 °C from 25 °C to 400 °C, and ±2 °C above 400 °C, respectively. The heating rate during testing typically ranged from 0.2 °C to 5 °C per minute, with a reduction to 0.2 °C per minute near phase transitions. To determine the salinity of the gas–liquid two-phase aqueous solution inclusions, ice-melting temperatures were employed [56], and the density of the fluid inclusions was calculated using Flincor software (version 1.4) [57]. Additionally, the volatile compositions of individual fluid inclusions were identified using a Renishaw RM-2000 Raman probe located at the Institute of Mineral Resources, Chinese Academy of Geological Sciences in Beijing, China. The excitation wavelength utilized was 514.53 nm from an argon laser, with a measurement spectrum time of 20 s. The counting rate remained consistent at one per centimeter, maintaining precision throughout. The laser beam was consistently set at a 1 μm size, offering a spectral resolution within the range of 1–2 $cm^{-1}$. Spectral data were acquired over the extensive wavenumber span of 1000–4000 $cm^{-1}$, ensuring comprehensive coverage.

### *4.4. H–O–C–Pb Isotope Analyses*

#### 4.4.1. H–O–C Isotope Analyses

All the samples were smashed at the Langfang Chengxin Geological Service Co., Ltd., Hebei Province, China. The mineral separates were extracted and handpicked under a binocular microscope to achieve a purity of 99%. Isotope analyses for H–O–C were conducted utilizing a MAT 251EM mass spectrometer located at the Beijing Research Institute of Uranium Geology in China. The analytical precision was outstanding, with results surpassing the following margins: ±2‰ for δD, ±0.2‰ for $\delta^{18}O$, and ±0.1‰ for $\delta^{13}C$. In the case of quartz, O isotope analysis was performed using the $BrF_5$ method to extract $CO_2$ [58]. The calcite samples reacted with phosphoric acid at 25 °C to produce $CO_2$ for the C–O isotope analyses of calcite. The H isotope of water in fluid inclusions of quartz and calcite was measured for vapors released from FIs in quartz and calcite grains with the thermal crack method. Hydrogen, produced by the reaction of the released water and zinc at 400 °C [59], was used for H isotope analysis. The $\delta^{18}O$ of water for quartz was calculated

from the O isotopes of quartz by using the fractionation equation 10001n $a_{quartz–water}$ = (3.38 × $10^6$) $T^{-2}$ − 3.40, and the $\delta^{18}O$ of water for calcite was calculated from the O isotopes of calcite by using the fractionation equation 10001n $a_{calcite–water}$ = (4.01 × $10^6$) $T^{-2}$ − (4.66 × $10^6$) $T^{-1}$ + 1.71 [60], where the $T$ (in Kelvin) represents the average fluid inclusion homogeneous temperature associated with the mineralization stage.

#### 4.4.2. Pb Isotope Analyses

The procedure for isolating individual sulfides followed the methodology outlined in Section 4.4.1. Subsequently, the Pb isotope composition of the sulfides was determined at the Analytical Laboratory of the Beijing Research Institute of Uranium Geology, China, using a GV IsoProbe-T multi-collector thermal ionization mass spectrometer. Remarkably, the measurement precision for both $^{208}Pb/^{206}Pb$ and $^{207}Pb/^{206}Pb$ ratios exceeded 0.005‰ (2σ). The isotopic ratios were reported relative to the Pb standard reference NBS-981 values, as follows: $^{206}Pb/^{204}Pb$ = 16.934 ± 0.007, $^{207}Pb/^{204}Pb$ = 15.486 ± 0.012, and $^{208}Pb/^{204}Pb$ = 36.673 ± 0.033, respectively [61].

## 5. Results

### *5.1. Syenogranite Zircon U–Pb Dating*

Fifteen zircon grains and twenty zircon grains from the syenogranite samples SJ49-1 and SJ49-10, respectively, were selected for LA-ICP-MS U–Pb dating. Zircon U–Pb compositions were analyzed based on the texture shown on CL images (Figure 8a,b). The analytical data are presented in Table 2 and are plotted on Concordia diagrams (Figure 8c,d).

**Table 2.** LA-ICP-MS zircon U–Pb dating data for the syenogranite in the Shuangjianzishan area.

| Spot No. | Isotopic Ratios | | | | | | Age (Ma) | | | |
|---|---|---|---|---|---|---|---|---|---|---|
| | $^{207}Pb/^{206}Pb$ | 1σ | $^{207}Pb/^{235}U$ | 1σ | $^{206}Pb/^{238}U$ | 1σ | $^{238}U/^{206}Pb$ | 1σ | $^{206}Pb/^{238}U$ | 1σ |
| Sample SJ49-1 | | | | | | | | | | |
| SJ49-1-5 | 0.05207 | 0.00419 | 0.15345 | 0.00467 | 0.02148 | 0.00034 | 145 | 11 | 137 | 3 |
| SJ49-1-6 | 0.05151 | 0.00219 | 0.15133 | 0.00427 | 0.02143 | 0.00029 | 143 | 6 | 137 | 2 |
| SJ49-1-7 | 0.05404 | 0.00366 | 0.15977 | 0.00201 | 0.02136 | 0.00036 | 151 | 11 | 136 | 2 |
| SJ49-1-8 | 0.05460 | 0.00363 | 0.16211 | 0.00490 | 0.02168 | 0.00035 | 153 | 9 | 138 | 3 |
| SJ49-1-9 | 0.04866 | 0.00210 | 0.14663 | 0.00447 | 0.02204 | 0.00039 | 139 | 6 | 141 | 2 |
| SJ49-1-10 | 0.05433 | 0.00359 | 0.16148 | 0.00411 | 0.02166 | 0.00032 | 152 | 10 | 138 | 3 |
| SJ49-1-11 | 0.05142 | 0.00149 | 0.15133 | 0.00442 | 0.02139 | 0.00030 | 143 | 4 | 136 | 2 |
| SJ49-1-12 | 0.05311 | 0.00273 | 0.15878 | 0.00418 | 0.02162 | 0.00034 | 150 | 7 | 138 | 2 |
| SJ49-1-13 | 0.05426 | 0.00331 | 0.16184 | 0.00580 | 0.02173 | 0.00033 | 152 | 9 | 139 | 5 |
| SJ49-1-14 | 0.05297 | 0.00267 | 0.15271 | 0.00588 | 0.02122 | 0.00037 | 144 | 6 | 135 | 2 |
| SJ49-1-15 | 0.05326 | 0.00183 | 0.16031 | 0.00529 | 0.02201 | 0.00032 | 151 | 5 | 140 | 2 |
| Sample SJ49-10 | | | | | | | | | | |
| SJ49-10-1 | 0.05360 | 0.00234 | 0.15744 | 0.00366 | 0.02150 | 0.00036 | 354 | 98 | 149 | 6 |
| SJ49-10-2 | 0.05298 | 0.00273 | 0.15447 | 0.00351 | 0.02152 | 0.00036 | 328 | 117 | 146 | 7 |
| SJ49-10-3 | 0.05103 | 0.00178 | 0.15186 | 0.00530 | 0.02159 | 0.00033 | 243 | 77 | 144 | 5 |
| SJ49-10-4 | 0.05306 | 0.00211 | 0.16012 | 0.00674 | 0.02171 | 0.00027 | 332 | 91 | 151 | 6 |
| SJ49-10-5 | 0.05211 | 0.00203 | 0.15586 | 0.00647 | 0.02165 | 0.00035 | 300 | 89 | 147 | 6 |
| SJ49-10-6 | 0.05381 | 0.00304 | 0.16331 | 0.00512 | 0.02198 | 0.00037 | 365 | 128 | 154 | 8 |
| SJ49-10-7 | 0.05146 | 0.00127 | 0.15120 | 0.00409 | 0.02123 | 0.00030 | 261 | 53 | 143 | 4 |
| SJ49-10-8 | 0.05294 | 0.00370 | 0.15308 | 0.00681 | 0.02095 | 0.00047 | 328 | 155 | 145 | 9 |
| SJ49-10-9 | 0.05087 | 0.00207 | 0.15079 | 0.00669 | 0.02135 | 0.00032 | 235 | 94 | 143 | 6 |
| SJ49-10-10 | 0.05095 | 0.00659 | 0.15175 | 0.00241 | 0.02123 | 0.00048 | 239 | 283 | 144 | 21 |
| SJ49-10-11 | 0.05309 | 0.00244 | 0.16196 | 0.00318 | 0.02201 | 0.00039 | 332 | 101 | 152 | 7 |
| SJ49-10-12 | 0.05295 | 0.00226 | 0.15167 | 0.00605 | 0.02077 | 0.00046 | 328 | 94 | 143 | 5 |
| SJ49-10-13 | 0.05161 | 0.00190 | 0.14800 | 0.00525 | 0.02093 | 0.00029 | 333 | 81 | 140 | 5 |
| SJ49-10-14 | 0.05390 | 0.00150 | 0.16319 | 0.00505 | 0.02185 | 0.00034 | 369 | 63 | 154 | 4 |
| SJ49-10-15 | 0.05386 | 0.00215 | 0.15455 | 0.00616 | 0.02084 | 0.00027 | 365 | 91 | 146 | 5 |
| SJ49-10-16 | 0.05468 | 0.00306 | 0.16463 | 0.00531 | 0.02207 | 0.00042 | 398 | 94 | 155 | 7 |
| SJ49-10-17 | 0.05391 | 0.00209 | 0.16044 | 0.00622 | 0.02162 | 0.00038 | 369 | 89 | 151 | 5 |
| SJ49-10-18 | 0.05461 | 0.00307 | 0.15926 | 0.00573 | 0.02129 | 0.00036 | 395 | 126 | 150 | 8 |
| SJ49-10-19 | 0.05024 | 0.00245 | 0.14607 | 0.00689 | 0.02130 | 0.00033 | 206 | 118 | 138 | 6 |
| SJ49-10-20 | 0.05368 | 0.00154 | 0.16087 | 0.00483 | 0.02167 | 0.00028 | 367 | 60 | 152 | 4 |

Zircon grains retrieved from the syenogranite exhibit euhedral–subhedral shapes and demonstrate distinctive oscillatory zoning in CL images (Figure 8a,b), which, combined with their relatively high Th/U ratios (0.25–0.58), indicates their magmatic origin. Fifteen analyses from sample SJ49-1 form a tight cluster on a concordial diagram and yield a weighted mean $^{206}Pb/^{238}U$ age of 137 ± 1.4 Ma (MSWD = 1.5; Figure 8c), and twenty analyses from sample SJ49-10 form a tight cluster on a concordial diagram and yield a weighted mean $^{206}Pb/^{238}U$ age of 137 ± 1.2 Ma (MSWD = 1.6; Figure 8d), suggesting that the syenogranite formed during the Early Cretaceous.

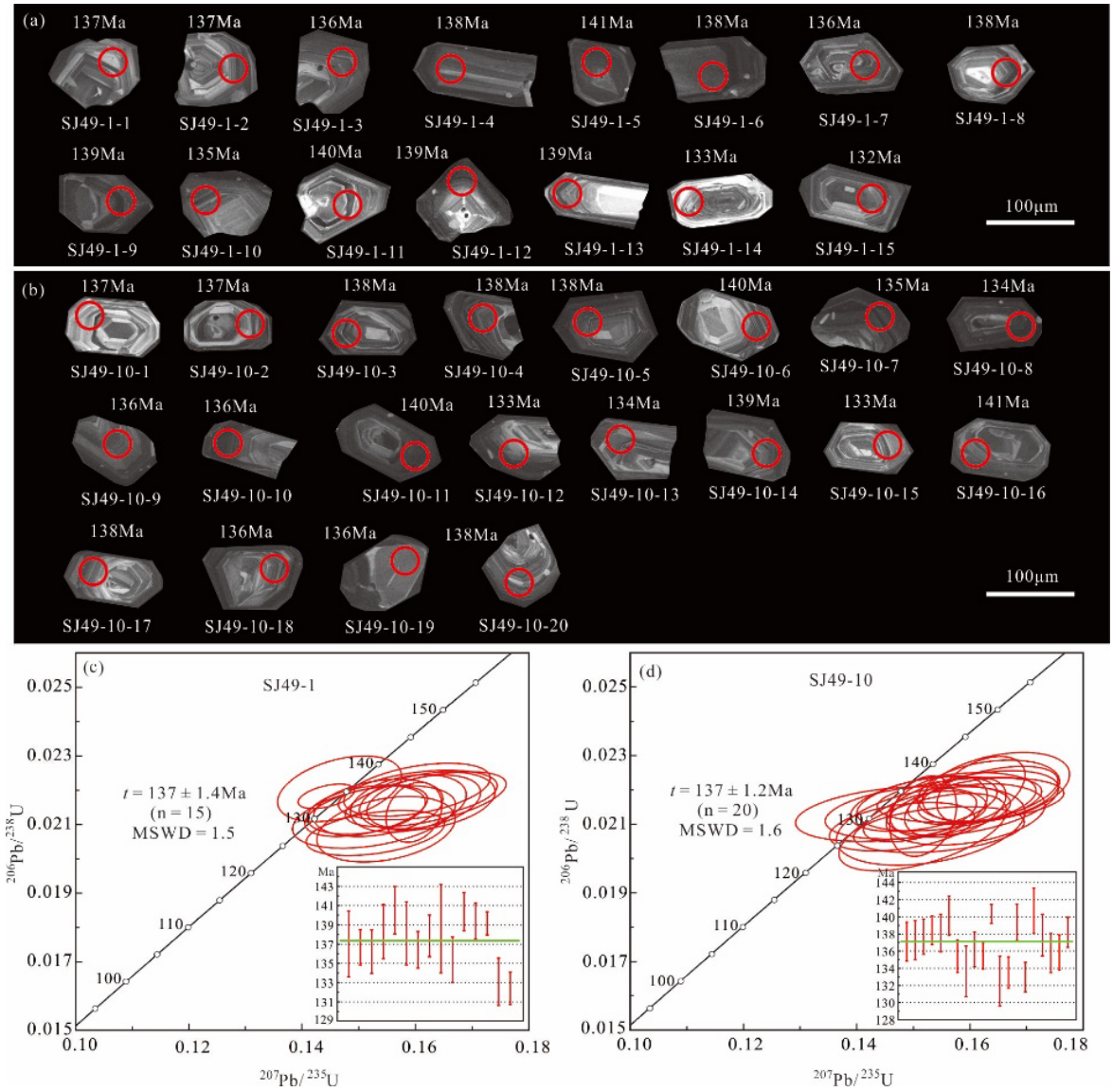


**Figure 8.** Representative cathodoluminescence (CL) images of zircon grains for samples sj49-1 (**a**) and sj49-10 (**b**) from the Shuangjianzishan syenogranite, showing U–Pb analytical spots and corresponding $^{206}Pb/^{238}U$ ages, and zircon U–Pb concordia diagrams of samples sj49-1 (**c**) and sj49-10 (**d**).

## *5.2. Fluid Inclusion Data*

### 5.2.1. Petrography

A fluid inclusion assemblage (FIA) is defined as a collection of fluid inclusions that were contemporaneously trapped, enabling us to obtain more reliable and precise data through fluid inclusion microthermometry using the FIA approach [62]. In this research, the

criteria put forth by Goldstein and Reynolds [62] were applied to designate fluid inclusions that occur in close proximity or isolated positions as having a primary origin, thereby classifying them as FIA. Here, we focus on the primary inclusions (Figure 9), of which there are four types in the Xinglongshan ore block, using criteria such as phase ratios at room temperature (21 °C), phase transitions observed during heating and cooling, and findings from laser Raman spectroscopy.

(1) Liquid-rich inclusions (WL-type): Within the examined quartz and calcite samples from all stages, these fluid inclusions are prevalent, constituting approximately 85% of the total number of inclusions. They exhibit elliptical, elongated columnar, and irregular shapes, with long axes ranging from 5 to 35 μm. Notably, the bubbles within them occupy 5%–45% of the total volume at room temperature (Figure 9a–f). When subjected to heating, these fluid inclusions underwent homogenization, transitioning into a liquid phase.

(2) Gas-rich inclusions (WG-type): Exclusively found in quartz from stage I, these inclusions make up approximately 5% of the total number of fluid inclusions, with long axes ranging from 45 to 60 μm. WG-type inclusions are typically oval or circular in shape, with bubbles occupying 55%–70% of their total volume (Figure 9b). Upon heating, these inclusions homogenized into a vapor phase.

(3) Pure gas inclusions (G-type): Predominantly present in quartz from stage I, these inclusions measure 5–10 μm in size and display irregular or round shapes (Figure 9a). They account for 3% of the total number of fluid inclusions and remain in a gaseous phase at room temperature, undergoing no phase change when heated.

(4) Pure liquid inclusions (L-type): Primarily hosted within quartz and calcite from stages III and IV, these inclusions exhibit irregular and negative crystal shapes and have a size of 5–10 μm (Figure 9f). They constitute approximately 7% of the total number of fluid inclusions and remain in a liquid phase at room temperature. Upon heating, the L-type inclusions do not undergo any phase change.

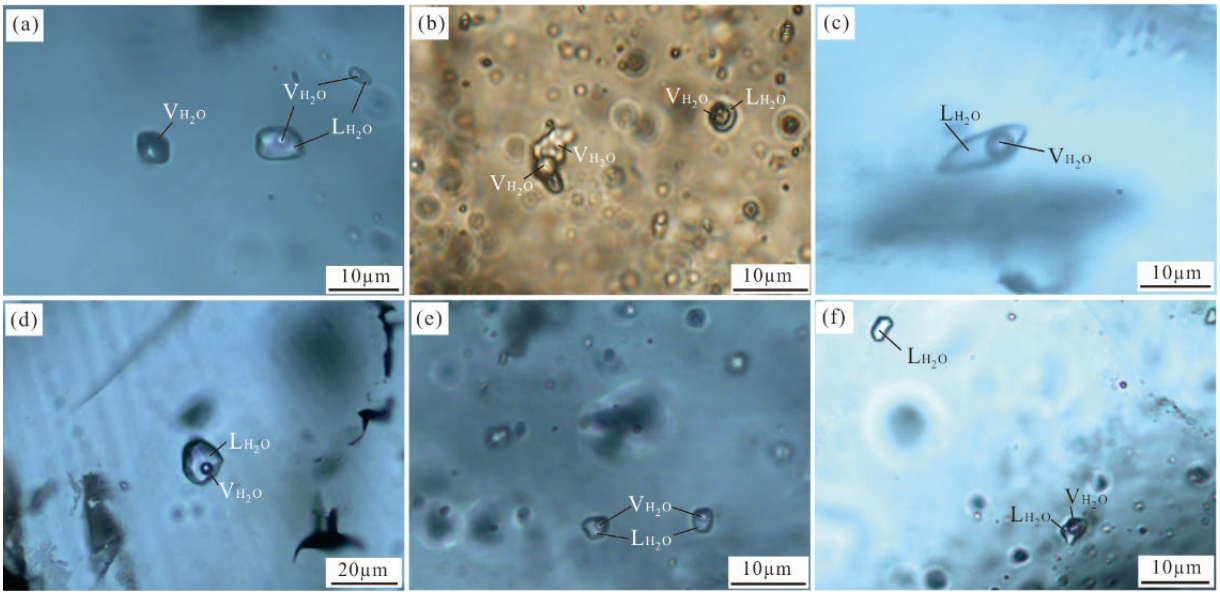


**Figure 9.** Illustrative microphotographs of fluid inclusions within quartz and calcite crystals sourced from the Xinglongshan ore block. (**a**) G- and WL-type FIs in quartz of stage I; (**b**) WG- and WL-type FIs in quartz of stage I; (**c**) WL-type FIs in quartz of stage II; (**d**) WL-type FIs in quartz of stage II; (**e**) WL-type FIs in quartz of stage III; (**f**) WL- and L-type FIs in calcite of stage IV. $L_{H2O}$ = liquid phase $H_2O$; $V_{H2O}$ = vapor phase $H_2O$.

5.2.2. Microthermometry

The microthermometric results, along with the parameters of the FIA, are presented in Table 3 and depicted in Figure 10.

(1) FIs in quartz of stage I (sample SJ14): Three FIAs have been recognized. The homogenization temperature of two WL-type FIAs varies from 253 °C to 302 °C (Figure 10a), and the final ice melting temperature is −3.2 °C to −1.9 °C, corresponding to salinities of 3.4–5.3 wt% NaCl eqv. (Figure 10b), and the density of the fluid is 0.74–0.83 g/cm$^3$. The homogenization temperature of one WG-type FIA varies from 279 °C to 289 °C, and the final ice melting temperature is −4.1 °C to −2.4 °C, corresponding to salinities of 4.0–6.6 wt% NaCl eqv., and the density of the fluid is 0.79–0.80 g/cm$^3$.

(2) FIs in quartz of stage II (samples SJ6 and SJ31): Three FIAs have been recognized. The homogenization temperature of these FIAs varies from 203 °C to 268 °C (Figure 10c), and the final ice melting temperature ranges from −4.5 °C to −1.6 °C, corresponding to salinities of 2.6–7.2 wt% NaCl eqv. (Figure 10d), and the fluid density is 0.80–0.88 g/cm$^3$.

(3) FIs in quartz and calcite of stage III (samples SJ11, SJ12, and SJ13-1): Three FIAs have been recognized. The homogenization temperature of two WL-type FIAs in quartz varies from 200 °C to 222 °C (Figure 10e), and the final ice melting temperature ranges from −3.5 °C to −1.8 °C, corresponding to salinities of 3.1–5.7 wt% NaCl eqv. (Figure 10f), and the fluid density is 0.86–0.91 g/cm$^3$. The homogenization temperature of one WL-type FIA in calcite varies from 184 °C to 199 °C, and the final ice melting temperature ranges from −4.4 °C to −1.7 °C, corresponding to salinities of 2.9–7.0 wt% NaCl eqv., and the fluid density is 0.89–0.92 g/cm$^3$.

(4) FIs in quartz and calcite of stage IV (samples SJ8 and SJ45): Two FIAs have been recognized. The homogenization temperature of one WL-type FIA in quartz varies from 185 °C to 198 °C (Figure 10g), and the final ice melting temperature ranges from −2.2 °C to −1.5 °C, corresponding to salinities of 2.6–3.7 wt% NaCl eqv. (Figure 10h), and the fluid density is 0.89–0.91 g/cm$^3$. The homogenization temperature of one WL-type FIA in calcite varies from 153 °C to 187 °C, and the final ice melting temperature ranges from −2.9 °C to −0.7 °C, corresponding to salinities of 1.2–4.8 wt% NaCl eqv., and the fluid density is 0.90–0.93 g/cm$^3$.

**Table 3.** Microthermometric data and relevant parameters of the fluid inclusion assemblage (FIA) in quartz and calcite from the Xinglongshan ore block.

| Type | Host Mineral | FIA No. | No. | Size (μm) | *V* (vol.%) | $T_{m\ (ice)}$ (°C) | $T_h$ (°C) | | Salinity (wt% NaCl Eqv.) | Density (g/cm$^3$) |
|---|---|---|---|---|---|---|---|---|---|---|
| | | | | | | Range | Range | Mean | Range | |
| Stage I: sphalerite–arsenopyrite–pyrite–chalcopyrite–quartz stage (sample SJ14) | | | | | | | | | | |
| WL | Quartz | 1 | 6 | 5–30 | 5–40 | −3.2 to −1.9 | 278–302 | 288 | 3.4–5.3 | 0.74–0.79 |
| WL | Quartz | 2 | 5 | 10–30 | 10–35 | −3.2 to −2.2 | 253–274 | 263 | 3.7–5.3 | 0.80–0.83 |
| WG | Quartz | 3 | 3 | 45–60 | 55–70 | −4.1 to −2.4 | 279–289 | 284 | 4.0–6.6 | 0.79–0.80 |
| Stage II: sphalerite–galena–pyrite–silver-bearing minerals–quartz stage (samples SJ6 and SJ31) | | | | | | | | | | |
| WL | Quartz | 4 | 11 | 5–30 | 10–25 | −4.5 to −2.5 | 224–248 | 238 | 3.9–7.2 | 0.84–0.88 |
| WL | Quartz | 5 | 16 | 10–35 | 5–45 | −4.2 to −1.6 | 229–268 | 238 | 3.2–6.7 | 0.83–0.87 |
| WL | Quartz | 6 | 6 | 10–30 | 5–20 | −2.3 to −1.8 | 203–221 | 220 | 2.6–3.9 | 0.80–0.88 |
| Stage III: sphalerite–galena–silver-bearing minerals–quartz–calcite stage (samples SJ11, SJ12, and SJ13-1) | | | | | | | | | | |
| WL | Quartz | 7 | 20 | 10–35 | 5–20 | −3.5 to −1.8 | 200–222 | 212 | 3.1–5.7 | 0.86–0.91 |
| WL | Quartz | 8 | 12 | 10–30 | 10–20 | −2.8 to −1.9 | 200–216 | 208 | 3.2–4.6 | 0.87–0.90 |
| WL | Calcite | 9 | 12 | 10–30 | 10–20 | −4.4 to −1.7 | 184–199 | 192 | 2.9–7.0 | 0.89–0.92 |
| Stage IV: weakly mineralized quartz–calcite stage (samples SJ8 and SJ45) | | | | | | | | | | |
| WL | Quartz | 10 | 4 | 15–20 | 5–20 | −2.2 to −1.5 | 185–198 | 191 | 2.6–3.7 | 0.89–0.91 |
| WL | Calcite | 11 | 9 | 10–35 | 10–20 | −2.9 to −0.7 | 153–187 | 176 | 1.2–4.8 | 0.90–0.93 |

Abbreviations: $T_{m\ (ice)}$ = final melting temperature of ice; $T_h$ = total homogenization temperature; *V* = volume fraction of gas phase in the total volume of inclusion.

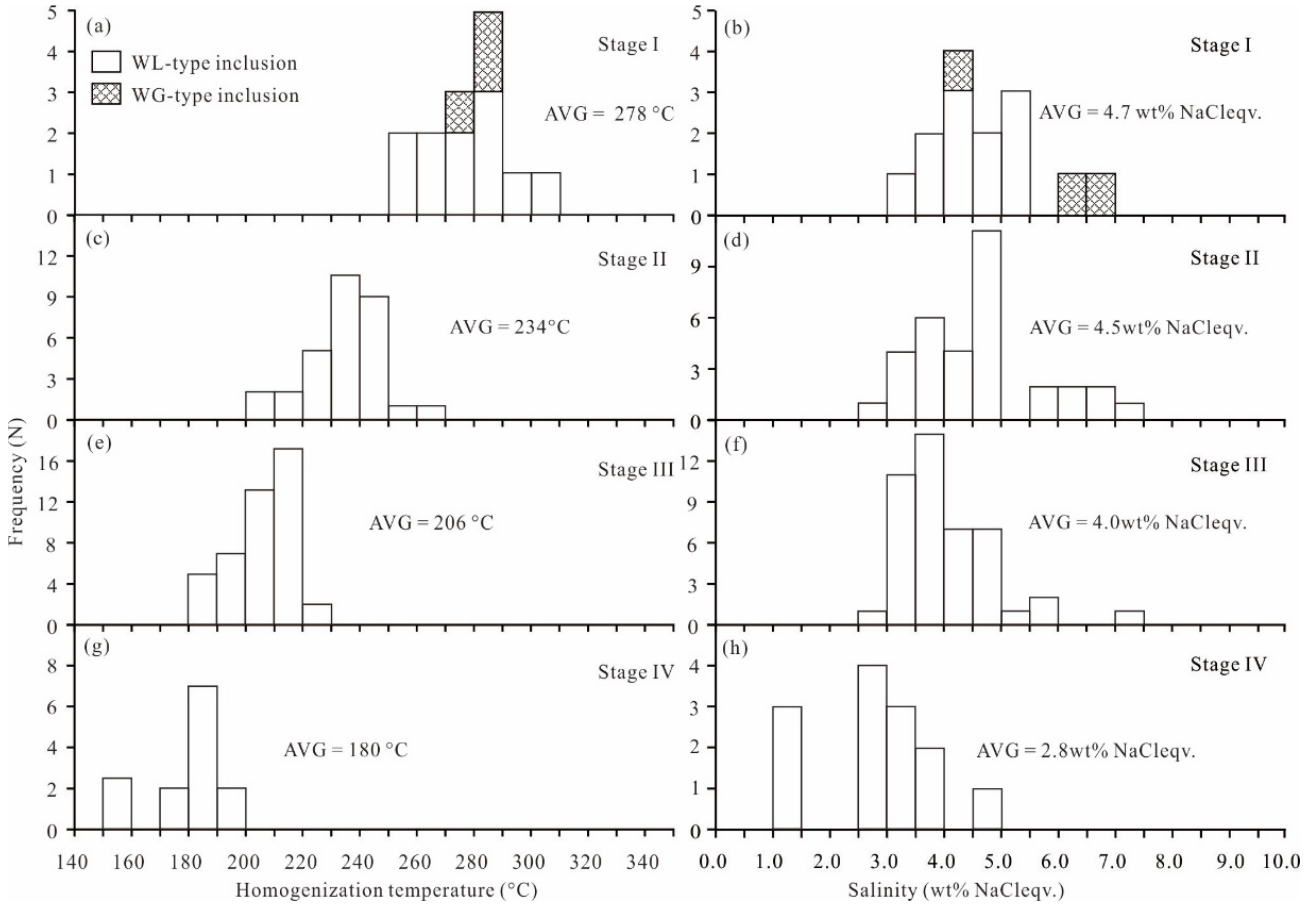


**Figure 10.** Histograms illustrating the homogenization temperatures and salinity of fluid inclusions within quartz and calcite from the Xinglongshan ore block. (**a**) Homogenization temperature of stage I; (**b**) salinity of stage I; (**c**) homogenization temperature of stage II; (**d**) salinity of stage II; (**e**) homogenization temperature of stage III; (**f**) salinity of stage III; (**g**) homogenization temperature of stage IV; (**h**) salinity of stage IV.

#### 5.2.3. Laser Raman Spectra

The results of comprehensive laser Raman spectroscopic examinations on individual fluid inclusions within quartz and calcite from various stages are visually represented in Figure 11. In stage I, the gas-phase composition of FIs primarily consists of $H_2O$, although an inconspicuous $CH_4$ peak is also displayed. For stages II and III, the gas-phase composition is predominantly $H_2O$. In stage IV, the gas-phase of FIs is mainly composed of $H_2O$ with a minor presence of $C_6H_6$. Overall, the ore-forming fluid is characterized as belonging to an $H_2O$–NaCl ± $C_6H_6$ system. Raman spectroscopy analysis shows that the ore-forming fluid of stages I, II, and III belongs to an $H_2O$–NaCl system and that the fluid of stage IV belongs to an $H_2O$–NaCl–($C_6H_6$) system. The presence of a small amount of $C_6H_6$ in stage IV indicates that the late meteoric water carries organic matter components from the strata into the ore-forming fluid.

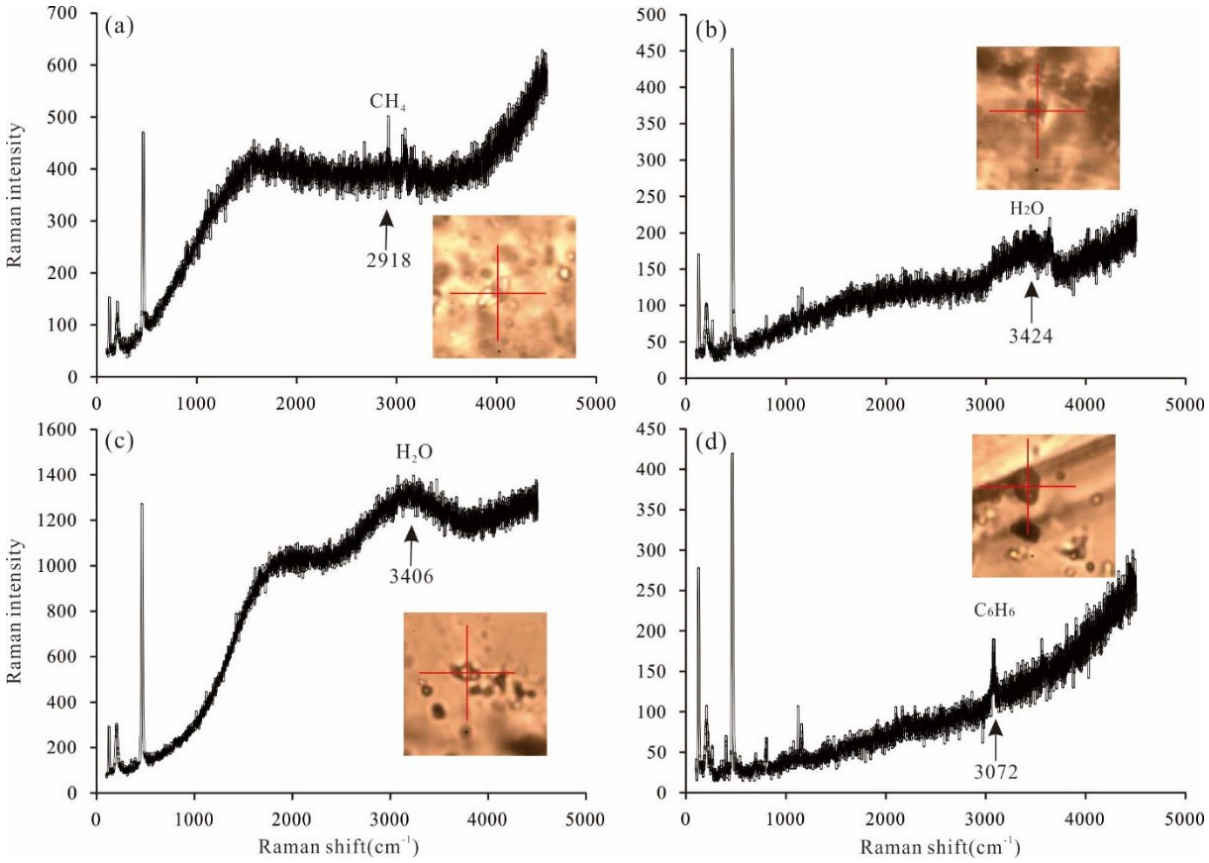


**Figure 11.** Laser Raman spectra for fluid inclusions in quartz and calcite from the Xinglongshan ore block. (**a**) Gas-phase composition of WL-type inclusions in quartz of stage I; (**b**) gas-phase composition of WL-type inclusions in quartz of stage II; (**c**) gas-phase composition of WL-type inclusions in quartz of stage III; (**d**) gas-phase composition of WL-type inclusions in calcite of stage IV.

### *5.3. Isotope Data*

#### 5.3.1. Hydrogen and Oxygen Isotopes

Isotope data for hydrogen and oxygen are presented in Table 4 and depicted in Figure 12. Within stage I, six quartz samples exhibit δD values ranging from −126‰ to −65‰, $\delta^{18}O_{quartz}$ values spanning 4.1‰ to 15.1‰, and $\delta^{18}O_{water}$ values ranging from −3.6‰ to 7.4‰. For stage II, four quartz samples display δD values between −118‰ and −94‰, $\delta^{18}O_{quartz}$ values in the range of 4.1‰ to 4.6‰, and $\delta^{18}O_{water}$ values from −5.6‰ to −3.6‰. In stage III, one quartz and four calcite samples yield δD values between −145‰ and −121‰, $\delta^{18}O_{mineral}$ values within the range of 1.0‰ to 7.4‰, and $\delta^{18}O_{water}$ values spanning −8.5‰ to −3.9‰. Similarly, within stage IV, two quartz and three calcite samples exhibit δD values ranging from −134‰ to −106‰, $\delta^{18}O_{quartz}$ values spanning from −0.8‰ to 7.9‰, and $\delta^{18}O_{water}$ values between −13.9‰ and −5.2‰. Notably, the$\delta^{18}O_{mineral}$ values of quartz samples (ranging from −0.8‰ to 15.1‰, mostly >4‰) in stages I to IV are generally higher than those of calcite samples (ranging from 1.0‰ to 4.5‰, mostly <3‰) from stages III to IV.

**Table 4.** Oxygen isotopic composition (‰) of quartz and calcite, hydrogen and oxygen isotopic compositions (‰) of fluid inclusions, and carbon isotopic composition (‰) of calcite from the Xinglongshan ore block.

| Sample No. | Mineral | Stage | $T_h$ (°C) | $\delta^{18}O_{quartz\ (V\text{-}SMOW)}$ | $\delta^{18}O_{water\ (V\text{-}SMOW)}$ | $\delta D_{V\text{-}SMOW}$ | $\delta^{13}C_{V\text{-}PDB}$ |
|---|---|---|---|---|---|---|---|
| 2-3m-3 | Quartz | I | 278 | 4.1 | −3.6 | −65 | |
| 8-16m-1 | Quartz | I | 278 | 5.8 | −1.9 | −75 | |

**Table 4.** *Cont.*

| Sample No. | Mineral | Stage | $T_h$ (°C) | $\delta^{18}O_{quartz\ (V\text{-}SMOW)}$ | $\delta^{18}O_{water\ (V\text{-}SMOW)}$ | $\delta D_{V\text{-}SMOW}$ | $\delta^{13}C_{V\text{-}PDB}$ |
|---|---|---|---|---|---|---|---|
| 1m-3 | Quartz | I | 278 | 5.8 | −1.9 | −126 | |
| 8-16m-3 | Quartz | I | 278 | 5.1 | −2.6 | −106 | |
| 8-16m-4 | Quartz | I | 278 | 5.1 | −2.6 | −120 | |
| 2-3m-7 | Quartz | I | 278 | 15.1 | 7.4 | −117 | |
| 2-3m-6 | Quartz | II | 234 | 4.1 | −5.6 | −97 | |
| 5#KD-2-1 | Quartz | II | 234 | 4.4 | −5.3 | −118 | |
| 5#KD-2-2 | Quartz | II | 234 | 4.5 | −5.2 | −103 | |
| 1-5-1m-2 | Quartz | II | 234 | 6.1 | −3.6 | −94 | |
| ZD4-1-1m-1 | Calcite | III | 206 | 2.5 | −7.0 | −133 | −11.0 |
| ZD4-1-1m-2 | Calcite | III | 206 | 1.9 | −7.6 | −138 | −10.7 |
| ZD4-1-1m-3 | Calcite | III | 206 | 1.0 | −8.5 | −145 | −10.5 |
| ZD4-1-1m-4 | Quartz | III | 206 | 7.4 | −3.9 | −123 | |
| ZD4-1-1m-4 | Calcite | III | 206 | 1.3 | −8.2 | −121 | −10.9 |
| 5#KD-1 | Quartz | IV | 180 | 7.9 | −5.2 | −106 | |
| 8-12m-1 | Calcite | IV | 180 | 4.5 | −6.5 | −123 | −9.9 |
| 8-12m-2 | Quartz | IV | 180 | −0.8 | −13.9 | −116 | |
| 8-12m-2 | Calcite | IV | 180 | 3.6 | −7.4 | −112 | −7.9 |
| 8-12m-3 | Calcite | IV | 180 | 2.5 | −8.5 | −134 | −9.4 |

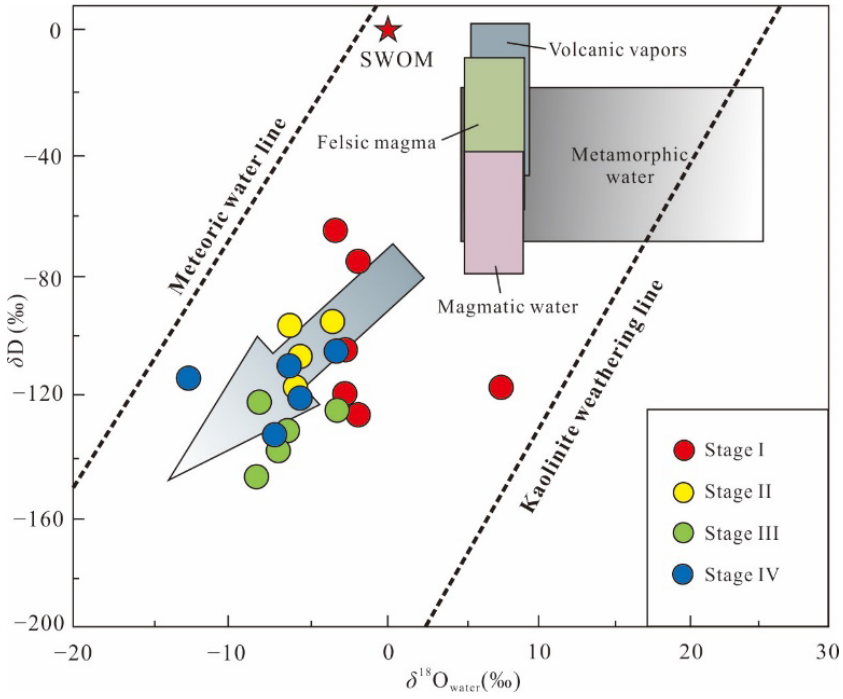


**Figure 12.** $\delta^{18}O_{water}$ versus $\delta D$ diagram of the Xinglongshan ore block (base map from [63]).

### 5.3.2. Carbon Isotope

Carbon isotope data are given in Table 4. Four calcite samples from stage III have $\delta^{13}C$ values of −11.0‰ to −10.5‰, and three calcite samples from stage IV have $\delta^{13}C$ values of −9.9‰ to −7.9‰.

### 5.3.3. Lead Isotope

The lead isotopic data for 21 sulfide samples are listed in Table 5. The $^{206}Pb/^{204}Pb$, $^{207}Pb/^{204}Pb$, and $^{208}Pb/^{204}Pb$ ratios for 3 galena, 3 sphalerite, and 3 pyrite samples from stage I are 18.285–18.361, 15.536–15.634, and 38.130–38.448, respectively. The $^{206}Pb/^{204}Pb$, $^{207}Pb/^{204}Pb$, and $^{208}Pb/^{204}Pb$ ratios for 1 galena and 1 sphalerite samples from stage II are 18.311–18.358, 15.567–15.630, and 38.234–38.438, respectively. The $^{206}Pb/^{204}Pb$, $^{207}Pb/^{204}Pb$,

and $^{208}Pb/^{204}Pb$ ratios for 1 galena, 1 sphalerite, and 1 pyrite samples from stage III are 18.278–18.310, 15.530–15.570, and 38.107–38.234, respectively. The $^{206}Pb/^{204}Pb$, $^{207}Pb/^{204}Pb$, and $^{208}Pb/^{204}Pb$ ratios for 2 galena, 2 sphalerite, and 2 pyrite samples from stage IV are 18.293–18.346, 15.564–15.616, and 38.229–38.389, respectively.

**Table 5.** Lead isotopic composition of sulfide samples from the Xinglongshan ore block.

| Sample No. | Mineral | Stage | $^{206}Pb/^{204}Pb$ | $^{207}Pb/^{204}Pb$ | $^{208}Pb/^{204}Pb$ | $t$ (Ma) | $\mu$ | $\omega$ | $\kappa$ | $\Delta\alpha$ | $\Delta\beta$ | $\Delta\gamma$ |
|---|---|---|---|---|---|---|---|---|---|---|---|---|
| 2-3m-1 | I | Galena | 18.308 | 15.569 | 38.229 | 137 | 9.31 | 35.5 | 3.69 | 65.2 | 15.9 | 26.1 |
| 2-3m-1 | I | Sphalerite | 18.285 | 15.536 | 38.130 | 137 | 9.29 | 35.1 | 3.65 | 63.9 | 13.7 | 23.5 |
| 2-3m-1 | I | Pyrite | 18.303 | 15.564 | 38.205 | 137 | 9.31 | 35.4 | 3.67 | 64.9 | 15.6 | 25.5 |
| 2m-3 | I | Galena | 18.361 | 15.634 | 38.448 | 137 | 9.37 | 36.3 | 3.75 | 68.3 | 20.1 | 32.0 |
| 2m-3 | I | Sphalerite | 18.290 | 15.545 | 38.179 | 137 | 9.29 | 35.3 | 3.67 | 64.2 | 14.3 | 24.8 |
| 2m-3 | I | Pyrite | 18.308 | 15.566 | 38.240 | 137 | 9.31 | 35.5 | 3.69 | 65.2 | 15.7 | 26.4 |
| 1m-1 | I | Galena | 18.355 | 15.626 | 38.419 | 137 | 9.36 | 36.2 | 3.75 | 67.9 | 19.6 | 31.2 |
| 1m-1 | I | Sphalerite | 18.323 | 15.585 | 38.261 | 137 | 9.33 | 35.6 | 3.69 | 66.1 | 16.9 | 27.0 |
| 1m-1 | I | Pyrite | 18.302 | 15.561 | 38.211 | 137 | 9.31 | 35.4 | 3.68 | 64.8 | 15.4 | 25.6 |
| ZD5-1-1m-1 | II | Galena | 18.358 | 15.630 | 38.438 | 137 | 9.36 | 36.3 | 3.75 | 68.1 | 19.9 | 31.7 |
| ZD5-1-1m-1 | II | Sphalerite | 18.311 | 15.567 | 38.234 | 137 | 9.31 | 35.5 | 3.69 | 65.4 | 15.8 | 26.2 |
| ZD4-1-1m-1 | III | Galena | 18.278 | 15.530 | 38.107 | 137 | 9.28 | 35.0 | 3.65 | 63.5 | 13.3 | 22.8 |
| ZD4-1-1m-1 | III | Sphalerite | 18.310 | 15.570 | 38.234 | 137 | 9.31 | 35.5 | 3.69 | 65.3 | 16.0 | 26.2 |
| ZD4-1-1m-1 | III | Pyrite | 18.299 | 15.555 | 38.199 | 137 | 9.30 | 35.3 | 3.68 | 64.7 | 15.0 | 25.3 |
| 8-16m-2 | IV | Galena | 18.311 | 15.569 | 38.239 | 137 | 9.31 | 35.5 | 3.69 | 65.4 | 15.9 | 26.4 |
| 8-16m-2 | IV | Sphalerite | 18.293 | 15.571 | 38.234 | 137 | 9.30 | 35.5 | 3.69 | 64.3 | 16.0 | 26.2 |
| 8-16m-2 | IV | Pyrite | 18.332 | 15.597 | 38.319 | 137 | 9.34 | 35.8 | 3.71 | 66.6 | 17.7 | 28.5 |
| 8-12m-1 | IV | Galena | 18.346 | 15.616 | 38.389 | 137 | 9.35 | 36.1 | 3.74 | 67.4 | 19.0 | 30.4 |
| 8-12m-1 | IV | Sphalerite | 18.329 | 15.598 | 38.331 | 137 | 9.33 | 35.9 | 3.72 | 66.4 | 17.8 | 28.9 |
| 8-12m-1 | IV | Pyrite | 18.307 | 15.564 | 38.229 | 137 | 9.31 | 35.5 | 3.69 | 65.1 | 15.6 | 26.1 |

Abbreviations: $\mu = {}^{238}U/{}^{204}Pb$; $\omega = {}^{232}Th/{}^{204}Pb$; $\kappa = Th/U$; $\Delta\alpha = [({}^{206}Pb/{}^{204}Pb)_{d(t)}/({}^{206}Pb/{}^{204}Pb)_{m(t)} - 1] \times 1000$; $\Delta\beta = [({}^{207}Pb/{}^{204}Pb)_{d(t)}/({}^{207}Pb/{}^{204}Pb)_{m(t)} - 1] \times 1000$; $\Delta\gamma = [({}^{208}Pb/{}^{204}Pb)_{d(t)}/({}^{208}Pb/{}^{204}Pb)_{m(t)} - 1] \times 1000$; d is the Pb of ore mineral; and m is mantle Pb calculated by Chen et al. [64].

## 6. Discussion

### *6.1. Timing of the Syenogranite and Mineralization*

Different attempts to date mineralization have been made in the last years, either by dating igneous rocks considered to be genetically related to mineralization or by dating hydrothermal alteration and ore minerals themselves. Cui [65] proposed that the age of Ag–Pb–Zn mineralization is 249 ± 2 Ma based on a zircon U–Pb age from one of the diorite dikes. Based on a zircon U–Pb date for granite porphyry that was believed to be related to the mineralization, Ouyang et al. [66] proposed an age of 159.3 ± 2.3 Ma. Wang [67] reported a U–Pb age of 148 ± 1 Ma for hydrothermal zircons. Wang et al. [37] indirectly dated the mineralization by determining the age of sericite using the Ar–Ar method and obtained an age of 147 ± 2 Ma. Zhai et al. [18] reported Re–Os ages of 135 ± 3.4 Ma for molybdenite and 135 ± 0.6 Ma for pyrite. Wu et al. [39] obtained an age of 133 ± 4 Ma from a sphalerite Rb–Sr isochron. Wang [67] used the Re–Os method on arsenopyrite and pyrite to obtain an age of 159 ± 6 Ma for the Ag–Pb–Zn mineralization. However, the wide range of the dating results shows that the age of the mineralization is still controversial.

The discovery of the concealed syenogranite by geophysical methods and drilling and evidence provided by the geophysical and geochemical models [68] suggest that the syenogranite intrusive is closely related to the mineralization and provide new insights into the timing of the mineralization processes. It can be seen from field observations that the syenogranite intrusion has undergone strong potassium and silicide alteration and contains many fine ore veins, as well as a large amount of potassium feldspar–quartz veinlets/stockworks and magmatic-hydrothermal breccias. Strong sericitization and silicification are seen in the contact between the intrusion and wall-rocks, and there are molybdenite–quartz ± albite fine veins and hydrothermal breccia zones in the local area [18]. The contact relationship between the syenogranite and mineralization suggests that the crystallization age of the syenogranite can be considered to be a pre-ore mineralization age close to the mineralization age. As described earlier, the concealed syenogranite yields a

zircon-weighted mean $^{206}Pb/^{238}U$ age of 137 Ma, which is basically consistent with the peak ages of the Early Cretaceous granites in the SGXR obtained from previous studies and suggests that the dioritic dike and the granite porphyry dated in earlier studies [65,66] are unlikely linked to the mineralization. Furthermore, this age is earlier than the average Re–Os model ages of molybdenite (135 ± 3.4 Ma) and pyrite (135 ± 0.6 Ma) reported by Zhai et al. [18] and the Rb–Sr isochron age of sphalerite (133 ± 4 Ma) reported by Wu et al. [68], thus, discarding ages determined from sericite [69], hydrothermal zircon, pyrite, and arsenopyrite [67]. Therefore, we infer that the mineralization age of the SJS deposit is not earlier than 137 Ma, and taking into account the above sphalerite, pyrite, and molybdenite dating results [18,37], an average 135 Ma age for the SJS deposit is likely to be a good estimation. This age is comparable to that of numerous other magmatic-hydrothermal ore deposits located in the SGXR, such as the Baiyinnuoer skarn Pb–Zn deposit (135 ± 1 Ma, [22]), the Bairendaba Ag–Pb–Zn deposit (135 ± 11 Ma, [70]), and the Weilasituo Sn–Li–Zn–Pb–Cu–Mo deposit (135 ± 7 Ma, [71]). Considering the U–Pb age of the syenogranite obtained by us in this study and previous dating results together, we conclude that the Early Cretaceous was an important mineralization period in the SJS ore district and that the vein-type Pb–Zn–Ag mineralization was closely related to granitic magma activity.

### *6.2. Source and Evolution of Ore-Forming Fluids*

The $\delta^{18}O_{water}$ and $\delta D$ values of the ore-forming fluids in the Xinglongshan ore block vary from −3.6‰ to 7.4‰ and −126‰ to −65‰ for stage I, −5.6‰ to −3.6‰ and −118‰ to −94‰ for stage II, −8.5‰ to −3.9‰ and −145‰ to −121‰ for stage III, and −13.9‰ to −5.2‰ and −134‰ to −106‰ for stage IV, respectively (Table 4). As shown in Figure 12, all samples, with a single exception, are plotted between the magmatic water box and the meteoric water evolution line. This feature indicates that the ore-forming fluid has a mixture source between magmatic and meteoric water and that the initial fluid may have derived from magmatic water. The $\delta^{18}O_{water}$ and $\delta D$ values of the Xinglongshan ore block are consistent with those of high-latitude meteoric water [71,72]. In addition, there is a gradually decreasing trend in H–O isotope composition from the early to late stage, indicating a continuous influx of meteoric water with the evolution of ore-forming fluids. This is also supported by C isotopic compositions. The $\delta^{13}C$ values of stages III and IV vary from −11.0‰ to −7.9‰ (mean −10.0‰). In general, there are three major carbon reservoirs on Earth: marine carbonate with a $\delta^{13}C$ mean of 0‰ [73]; carbonatite with $\delta^{13}C$ values varying from −7‰ to −3‰, averaging −5‰ [73,74]; and organic matter having a $\delta^{13}C$ mean of −25‰ [75]. The carbon isotope composition of the ore block is significantly different from that of marine carbonate and organic matter but slightly lower than that of carbonatite or granite. Given the geological context, we suggest that the carbon mainly came from granitic magma rather than carbonatites. In the $\delta^{18}O_{calcite}$–$\delta^{13}C_{V\text{-}PDB}$ diagram (Figure 13), all samples are projected on the left side of the C–O isotope composition region of igneous rocks, which is similar to the C–O isotope compositions reported by Zhang et al. [40] and Wang et al. [37] (Figure 13). The $\delta^{13}C$ value of atmospheric $CO_2$ ranges from −11‰ to −7‰ proposed by Hoefs [76]. In addition, compared to magmatic water, meteoric water has lower $\delta^{13}C$ values. Therefore, the involvement of meteoric water will cause the C–O isotope composition of the ore-forming fluid to migrate toward the lower left. Therefore, the C–O isotope composition of the ore-forming fluid in the Xinglongshan ore block shows a mixing of magmatic and meteoric water, indicating that the initial ore-forming fluid came from magma and mixed with meteoric water with the evolution of ore-forming fluid.

The laser Raman spectroscopy results indicate that the ore-forming fluid of the Xinglongsahn ore block overall belongs to an $H_2O$–NaCl–($C_6H_6$) system. The FIs in stage I, mainly consisting of WL-type with minor WG-type, are characterized by medium–high temperature (mean 278 °C) and low salinity (mean 4.7 wt% NaCl eqv.). The FIs in stages II and III, predominantly composed of WL-type, are featured by medium–low temperature

(mean 234 °C for stage II and mean 206 °C for stage III) and low salinity (mean 4.5 wt% NaCl eqv. for stage II and mean 4.0 wt% NaCl eqv. for stage III). The FIs in stage IV, mainly consisting of WL-type, have low temperature (mean 180 °C) and low salinity (mean 2.8 wt% NaCl eqv.). It should be noticed that the coexisting WL- and WG-type FIs were developed in stage I, while only WL-type FIs occurred in stages II, III, and IV. The homogenization temperature and salinity of the ore-forming fluid in the main mineralization stage (stages II and III) of the Xinglongshan ore block are consistent with the previous study [40], in which the homogenization temperature and salinity range from 201 °C to 280 °C and 0.5 wt% NaCl eqv. to 8.4 wt% NaCl eqv., respectively, indicating that this ore block mainly formed in a medium- to low-temperature and low salinity environment. The evolution of the system from early to late stage indicates that the temperature gradually decreases and that the salinity slightly changes but still shows a downward trend (Figures 10 and 14).

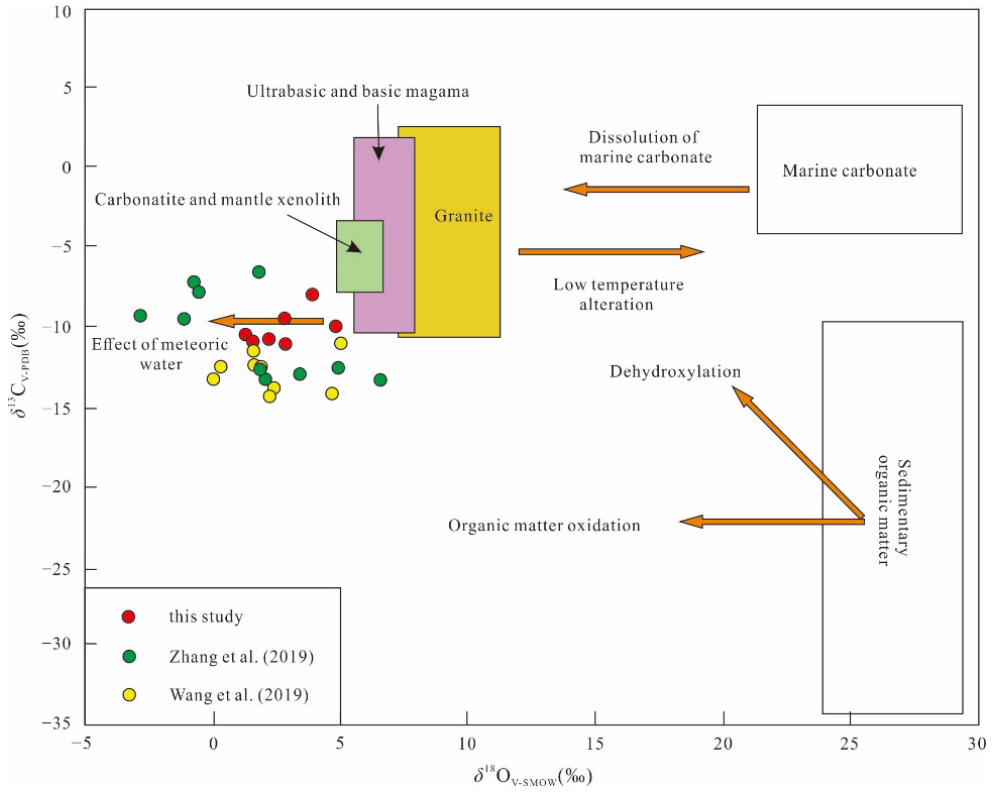


**Figure 13.** $\delta^{18}O$ versus $\delta^{13}C$ diagram of calcite from stages III and IV of the Xinglongshan ore block (base map from [37,40]).

In summary, the initial fluid of the Xinglongshan ore block was derived from magma, the ore-forming fluid is characterized by a mixture of magmatic and meteoric water, and the involvement of meteoric water gradually increased with the evolution of ore-forming fluids. Additionally, the homogenization temperature of the ore-forming fluid gradually decreases from stage I to stage IV, while the salinity is nearly constant, except for a significant decrease in stage IV (Figure 14). Overall, the ore-forming fluid is featured by medium–low temperature and low salinity and roughly belongs to an $H_2O$–NaCl ± $C_6H_6$ system.

### *6.3. Sources of Ore-Forming Materials*

The Pb isotopic composition is rarely fractionated in the processes of elemental migration and precipitation. Thus, it can be used to trace the source of metallogenic materials [77–81]. The μ, ω, and κ values of the Pb isotope for crust and mantle are 9.60 and 8.92, 36.84 and 31.84, and 5.85 and 3.45, respectively [82]. These values of the Xinglongshan ore block are 9.28–9.37, 35.0–36.3, and 3.65–3.75, with mean values of 9.32, 35.6, and 3.70,

respectively (Table 5), which are between those of crust and mantle. This feature implies that Pb was derived from a mixed source of the crust and mantle. In Figure 15a, all samples are plotted between the upper crust and mantle evolution curves, forming a steep straight line crossing the evolution line of the orogenic belt; in Figure 15b, all samples are projected between the lower crust and orogenic belt evolution lines and near the orogenic belt evolution line. The Pb isotopic composition of the Xinglongshan ore block indicates that Pb was derived from an orogenic belt or a mixed source of mantle and crust.

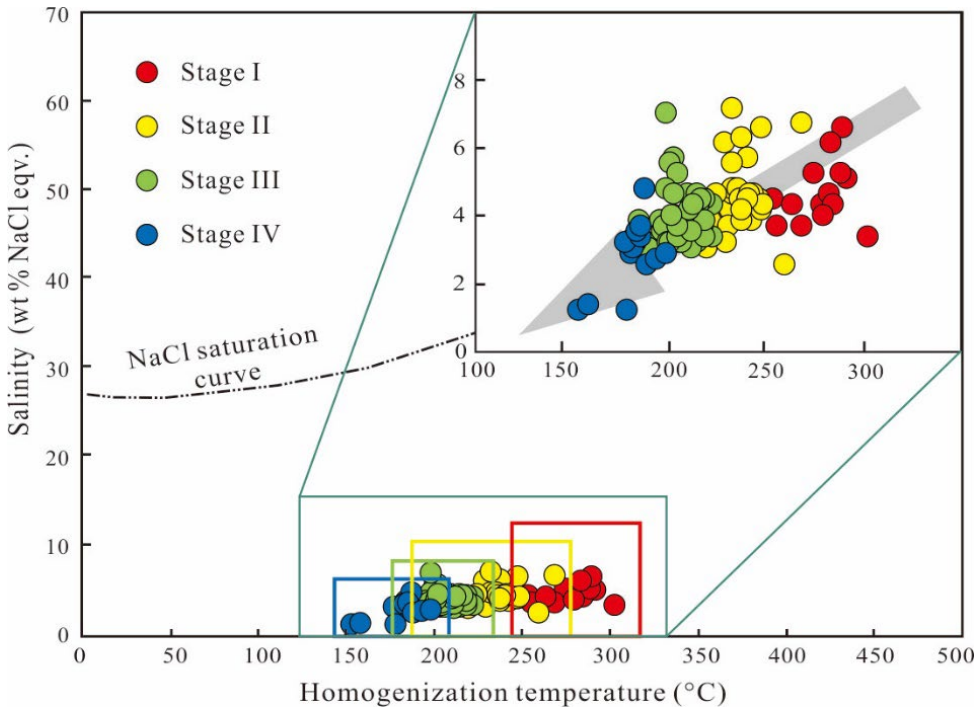


**Figure 14.** Diagram of homogenization temperature versus salinity of FIs in quartz and calcite from the Xinglongshan ore block. NaCl saturation curve from [56].

Zhu et al. [83] proposed that combining $\Delta\beta$ and $\Delta\gamma$ values can distinguish the tectonic backgrounds from which the ore minerals originated. In Figure 16, these data points of the Xinglongshan ore block are projected into the domain of magmatism, where the lead isotope composition has the characteristics of mixed lead sources from the upper crust and mantle [83]. Given that the SGXR was in an extensional background during the Early Cretaceous [14,27], we suggest that the ore-related magma originated from the mixing of depleted mantle- and crustal-derived magmas. Moreover, this primitive magma underwent the MASH (melting-assimilation-storage-homogenization) process in the lower crust, as proposed by Richards [84]. Wang et al. [28] reported the $\delta^{34}S$ values of 28 sulfide samples from the Xinglongshan ore block, ranging from −4.70‰ to 1.40‰. Zhai et al. [18] obtained 77 in situ sulfur isotope data for sulfides and Ag-bearing sulfosalts from the ore block, and their $\delta^{34}S$ values vary from −4.67‰ to 2.44‰, with a mean value of −2.11‰. The sulfur isotope composition of the Xinglongshan ore block is consistent with that of the magmatic and meteorite, indicative of a magmatic sulfur source.

In summary, the lead isotope composition obtained in this study and the sulfur isotope composition obtained by predecessors suggest that the ore-forming material of the Xinglongshan ore block mainly came from granitic magma.

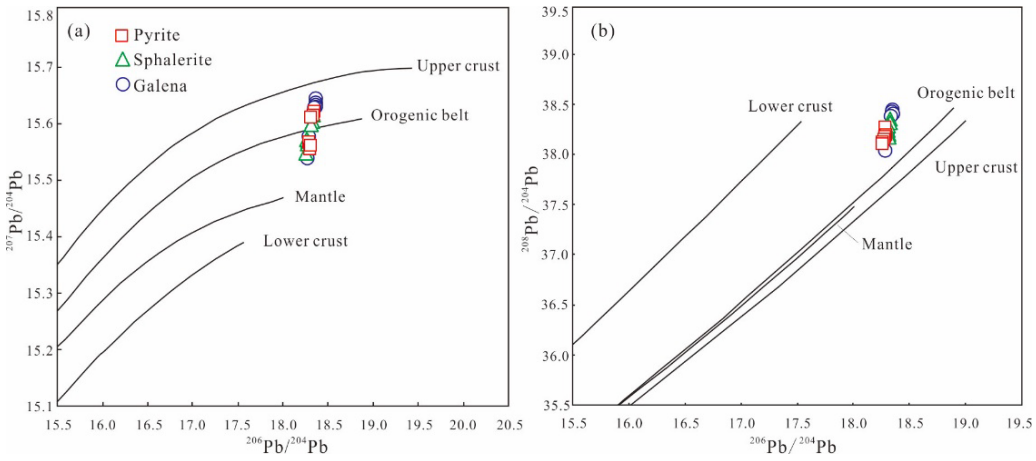


**Figure 15.** Diagrams of $^{206}Pb/^{204}Pb$ versus $^{207}Pb/^{204}Pb$ (**a**) and $^{206}Pb/^{204}Pb$ versus $^{208}Pb/^{204}Pb$ (**b**) for sulfides from the Xinglongshan ore block (base map from [82]).

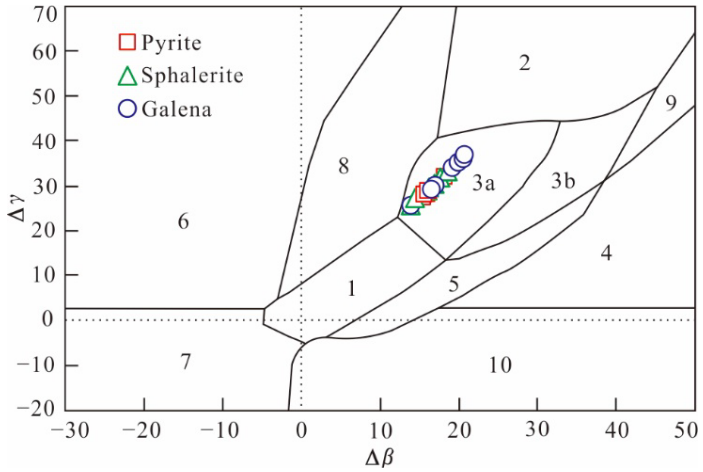


**Figure 16.** Δβ versus Δγ genetic classification diagram for lead isotopes of ore minerals from the Xinglongshan ore block (base map after [83]). Names of the number: 1 = mantle-derived lead; 2 = upper crust lead; 3 = subduction zone lead originated from the mixing of the upper crust and mantle lead (3a = lead related to magmatism; 3b = lead related to sedimentation); 4 = chemically deposited lead; 5 = submarine hydrothermal lead; 6 = medium–high grade metamorphism lead; 7 = lower crust lead of high-grade metamorphism; 8 = orogenic belt lead; 9 = upper crust lead in ancient shale; 10 = retrograde metamorphism lead.

### *6.4. Mechanism of Mineral Deposition*

The sulfides of the Xinglongshan ore block are dominated by sphalerite, galena, pyrite, chalcopyrite, and pyrrhotite, and no sulfate minerals were detected, indicating that $H_2S$ dominated the hydrothermal system with a low oxygen fugacity during the mineralization. The mean homogenization temperatures of FIs are 278 °C for stage I, 234 °C for stage II, 206 °C for stage III, and 180 °C for stage IV, respectively, indicating that the ore block formed in a medium–low temperature hydrothermal environment. The ore-forming fluid is characterized by low salinity, with salinities of 4.7 wt% NaCl eqv. for stage I, 4.5 wt% NaCl eqv. for stage II, 4.0 wt% NaCl eqv. for stage III, and 2.8 wt% NaCl eqv. for stage IV, respectively. Silver mainly exists in the form of $Ag^+$ in hydrothermal fluids and preferentially bonds with $HS^-$ [85], and in S-bearing systems, $Ag(HS)_2^-$ is the main species up to $T$ = 300–400 °C and $P$ = 50 MPa [86]. $Pb(HS)_2^0$ is the main Pb complex in a reduced hydrothermal fluid system under the conditions of low salinity (3.4 wt% NaCl eqv.), a temperature between 150 °C and 500 °C, and pressure greater than 100 MPa [66]. In a

low salinity and reduced hydrothermal fluids system, $Cu^{+}$ is the dominant form of Cu, forming strong complexes with $HS^{-}$ [87]. As for zinc, considering the low salinity of the ore-forming fluid, we speculate that it mainly exists in the form of Pb $(HS)_2^0$, although some researchers proposed that $ZnCl^{+}$ is the main Zn species in low salinity (3.4 wt% NaCl eqv.) hydrothermal fluid under the conditions of temperature ranging from 200 °C to 400 °C and pressure greater than 100 MPa [87,88]. In summary, the ore-forming elements, such as Ag, Pb, Zn, and Cu in the Xinglongshan ore block migrate in the form of hydrosulfide complexes.

The following mechanisms may cause the decomposition of complex, inducing mineral precipitation from solution [89–92]: (1) temperature decrease, (2) fluid immiscibility or boiling, (3) fluid mixing/dilution, and (4) fluid/rock interaction. The H–O isotopic compositions indicate that the mixture of magmatic and meteoric water took place during the mineralization of the Xinglongshan ore block (Figure 12); thus, fluid mixing is one of the main mechanisms for mineral precipitation. The homogenization temperatures of FIs from stage I to stage IV gradually decrease (Figure 13), implying that fluid cooling is also one of the mineral precipitation mechanisms. The quartz veins from stage I consist of WL- and WG-type FIs. These FIs coexist in the same quartz matrix (Figure 6b) and have similar homogenization temperatures and different salinities (Figure 10a,b). The WL-type FIs were homogenized to liquid, and the WG-type ones were homogenized to vapor when heated. The FIs of stage I exhibit typical features of fluid immiscibility. The Xinglongshan ore block belongs to a medium- to low-temperature hydrothermal deposit, and its $\delta^{13}C$ values range from −11.0‰ to −7.9‰, which is slightly lower than that of carbonatite (mean −5.0‰), but much higher than that of organic matter (mean −25‰). Therefore, we infer that the fluid–rock interaction was not the main mechanism of mineral precipitation in the ore block. Given the supergiant size of the SJS deposit, we do not believe that simple cooling is an efficient mechanism of ore precipitation because it does not sharply change the stability conditions of the complexes. In brief, fluid mixing was the main mechanism for mineral precipitation in the Xinglongshan ore block, despite the presence of a small amount of fluid immiscibility in stage I.

### *6.5. Ore Deposit Type and Metallogenic Model*

The genetic type of the SJS deposit has always been controversial, with two main viewpoints: epithermal type [18,28,40] and magmatic-hydrothermal vein type [27,33,68]. The main difference between the two views is whether the igneous rocks related to mineralization are granites, subvolcanic rocks, or porphyry intrusives. Zhai et al. [18] considered that the SJS mineralization is related to a granite porphyry, where shallow Ag–polymetallic vein ores and deep disseminated Mo ores form a porphyry Mo and epithermal Ag–polymetallic mineralization system. Jiang et al. [93] argued that the mineralization of the deposit is related to a highly-fractionated syenogranite and belongs to a magmatic-hydrothermal vein-type deposit. Zhao et al. [94] also deemed that the deposit belongs to a magmatic-hydrothermal vein-type deposit, but they thought that the mineralization is related to a highly-fractionated quartz syenite porphyry. The ore-forming fluid of the Xinglongshan ore block is characterized by medium–low temperature and low salinity, with a mineralogical assemblage including sphalerite, galena, arsenopyrite, pyrite, pyrrhotite, chalcopyrite, and silver-bearing sulfosalt minerals. These are typical characteristics of intermediate sulfidation epithermal (IS) deposits proposed by Chinchilla et al. [95] and Wang et al. [17]. Our study using field and microscopic investigation showed that the concealed granitic intrusive rocks in the Xinglongshan ore block have obvious granitic and porphyritic-like textures but do not show porphyritic structures. From bottom to top, the granitic complex consists of coarse-grained granite, medium to coarse-grained syenite granite, and fine-grained biotite granite (Figures 3c and 7). These indicate that the mineralization of the ore block is genetically related to granitic plutons and that the ore-forming depth is relatively deep. The main types of Ag–Sn–polymetallic deposits in the SGXR are classified into skarn, epithermal, and magmatic-hydrothermal vein types [14,27,30]. Of

them, deposits of magmatic-hydrothermal vein and skarn types are genetically related to granitic intrusions, while epithermal deposits are related to subvolcanic rocks [27]. Except for a small amount of porphyry Cu–Mo deposits, such as the Banlashan Cu–Mo, Aolunhua Mo–Cu, and Laojiagou Mo–polymetallic deposits, occurring on the eastern slope of the SGXR, no significant porphyry deposits occur on the main ridge and western slope of the SGXR, which, by contrast, is a huge Ag–Sn–polymetallic metallogenic belt characterized by magmatic-hydrothermal veins and epithermal deposits [27]. It is worth noting that in the same mining area, magmatic-hydrothermal vein-type and epithermal deposits often occur simultaneously, such as Baiyinchagandongshan, where the Baiyinchagandongshan magmatic-hydrothermal vein-type Ag–Sn–polymetallic and the Budunwula epithermal Ag–Pb–Zn deposits are developed [14]. In fact, the magmatic-hydrothermal vein-, porphyry-, and epithermal-type deposits in a region usually belong to the same magmatic-hydrothermal system [96], and the determination of different types of deposits mainly depends on their respective formation depths. Sillitoe [96] referred to vein ores that occur within noncarbonate rocks on the lateral to porphyry intrusives as subepithermal deposits. Strictly speaking, these vein deposits are not considered epithermal since they form in a deeper environment (lateral to a porphyry intrusive), although in common with IS epithermal veins, they also form from IS-type fluids and, therefore, can share similar mineralogy and alteration patterns [16]. Our study shows that the mineralization of the Xinglongshan ore block is closely related to the syenogranite and that it belongs to a magmatic-hydrothermal vein-type deposit; the mineralization of the Shuangjianzishan ore block is closely related to the Early Cretaceous subvolcanic rocks and that it belongs to an IS epithermal deposit. We therefore conclude that the Ag–Pb–Zn mineralization at Shuangjianzishan is genetically related to granites and subvolcanic rocks and that it belongs to a magmatic-hydrothermal vein–epithermal metallogenic system rather than a porphyry–epithermal metallogenic system.

Based on the above views, we establish a metallogenic model of volcanic–intrusive complex system to explain the Ag–Pb–Zn mineralization at Shuangjianzishan (Figure 17). Details are as follows:

During the Early Cretaceous, the rollback of the subducted Paleo-Pacific plate resulted in an extensional environment in the SGXR, triggering asthenospheric mantle upwelling [14,27,30]. Mantle-derived basaltic magma underplated beneath the lower crust, leading to partial melting of the crust. Crustal-derived magma mixed with mantle-derived magma to form crust–mantle mixed magma, and the mixed magma rose to the shallow part to form magma chambers [27,30]. The magma underwent fractional crystallization in the shallow magma chamber, forming metal-bearing granitic magma. The metal-bearing magma further rose, forming hypabyssal granitic intrusions. Ore-forming fluid exsolved from the ore-bearing granite mixed with meteoric water, leading to the precipitation of ore-forming materials within the preexisting faults, forming magmatic-hydrothermal vein-type Ag–polymetallic orebodies in the Xinglongshan ore block (Figure 17a). The metal-bearing granitic magma further rose, forming volcanic rocks on the surface and subvolcanic cupolas in volcanic edifices. Ore-forming fluid separated from the subvolcanic cupola mixed with meteoric water, resulting in mineral precipitation to form IS epithermal Ag-dominated Ag–Pb–Zn orebodies in the Shuangjianzishan ore block (Figure 17a). The Early Cretaceous volcanic rocks and intrusive rocks, sharing a common magma chamber, constitute coeval volcanic–intrusive complexes, forming a magmatic-hydrothermal vein-type and epithermal Ag–Pb–Zn–Cu–Sn metallogenic system related to granites and subvolcanic rocks at Shuangjianzishan (Figure 17b).

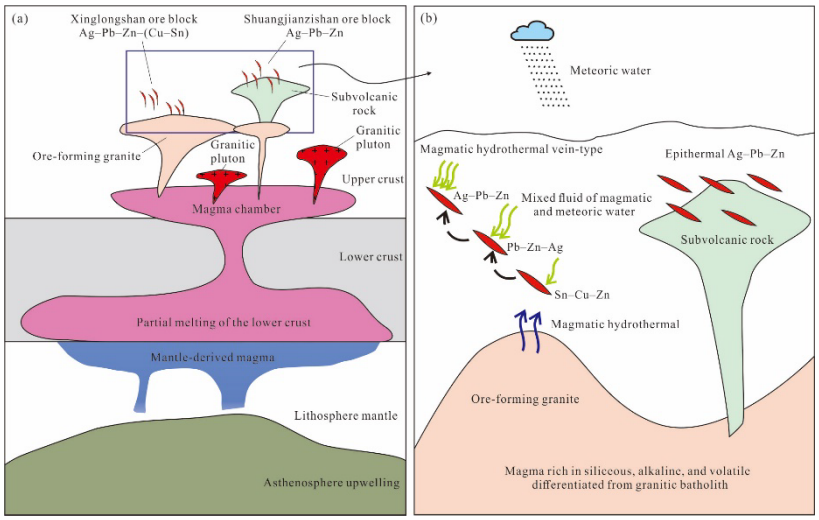


**Figure 17.** Metallogenic model of the SJS deposit. (**a**) magmatic-hydrothermal vein-type Ag–polymetallic orebodies in the Xinglongshan ore block. (**b**) magmatic-hydrothermal vein-type and epithermal Ag–Pb–Zn–Cu–Sn metallogenic system.

## 7. Conclusions

(1) The concealed syenogranite genetically related to the mineralization of the Xinglongshan ore block formed at approximately 137 Ma.

(2) The ore-forming fluid of the Xinglongshan ore block originated from a mixture of magmatic and meteoric water. With the evolution of ore-forming fluid, the amount of meteoric water increased gradually. The ore-forming fluid is characterized by medium–low temperature and low salinity and has an affinity of $H_2O$–NaCl ± $CH_4$ ± $C_6H_6$ in composition.

(3) The ore-forming material dominantly came from the Early Cretaceous granitic magma. Fluid mixing was the main mechanism for mineral precipitation.

(4) The Xinglongshan ore block belongs to a magmatic-hydrothermal vein-type deposit related to the Early Cretaceous syenogranite, and the Shuangjianzishan ore block belongs to an intermediate sulfidation epithermal deposit related to subvolcanic rocks. The Ag–Pb–Zn mineralization at Shuangjianzishan was genetically closely related to the Early Cretaceous volcanic–intrusive complex.

**Author Contributions:** Conceptualization, J.S. and G.W.; methodology, J.S.; software, J.S. and G.C.; validation, G.W.; formal analysis, J.S., G.C., F.Y. and G.C.; writing—original draft preparation, J.S.; writing—review and editing: G.W.; investigation, J.S., G.C. and B.J.; resources, W.L. and G.W.; data collection, T.Z, J.S. and B.J.; data curation: G.W. and T.Z.; visualization, G.C. and J.S.; supervision, G.W. and W.L; project administration and funding acquisition, G.W. All authors have read and agreed to the published version of the manuscript.

**Funding:** This research was financially supported by the National Natural Science Foundation of China (Grant No. 42372111), the Geological Survey Project of Copper and Gold Mineral Resources in Key Metallogenic Zones (Grant No. DD20230287), and the Scientific Research Project of Inner Mongolia Yulong Mining Co., Ltd. (Grant No. 2020110033002072).

**Data Availability Statement:** Data are contained within the article.

**Acknowledgments:** We would like to thank Engineers Xuejiao Li, Jing Zhao, Jie Yan, Tingting Zhang, and Yaling Wei from the Inner Mongolia Institute of Geological Survey for their participation during the field geological survey.

**Conflicts of Interest:** The authors declare no conflicts of interest.

## References


1. Gulson, B.L. Differences in lead isotope composition in the stratiform McArthur zinc–lead–silver deposit. *Miner. Deposita* **1975**, *10*, 277–286. [CrossRef]
2. Beaudoin, G.; Sangster, D.F. A descriptive model for silver–lead–zinc veins in clastic metasedimentary terranes. *Econ. Geol.* **1992**, *87*, 1005–1021. [CrossRef]
3. Leach, D.L.; Bradley, D.C.; Huston, D.; Pisarevsky, S.A.; Taylor, R.D.; Gardoll, S.J. Sediment-hosted lead–zinc deposits in Earth history. *Econ. Geol.* **2010**, *105*, 593–625. [CrossRef]
4. Wei, C.; Ye, L.; Huang, Z.L.; Gao, W.; Hu, Y.S.; Li, Z.L.; Zhang, J.W. Ore Genesis and Geodynamic Setting of Laochang Ag–Pb–Zn–Cu Deposit, Southern Sanjiang Tethys Metallogenic Belt, China: Constraints from Whole Rock Geochemistry, Trace Elements in Sphalerite, Zircon U–Pb Dating and Pb Isotopes. *Minerals* **2018**, *8*, 516. [CrossRef]
5. Yu, P.P.; Zheng, Y.; Wang, C.M. Trace elemental and sulfur–lead isotopic variations in metamorphosed volcanogenic massive sulfide (VMS) mineralization systems: An example from the Keketale Pb–Zn (–Ag) deposit, NW China. *Ore Geol. Rev.* **2020**, *125*, 103685. [CrossRef]
6. Sun, C.; Yang, X.Y.; Zhang, H.S.; Ji, W.H.; Chen, B.; Dong, Z.C.; Faisal, M.; Xi, D.H. Tracing the formation and modification of the Keketale VMS-type Pb–Zn deposit, Altai Mountains: Insights from ore deposit geology, geochronology, and magnetite geochemistry. *Ore Geol. Rev.* **2022**, *144*, 104852. [CrossRef]
7. Cooke, D.R.; Bull, S.W.; Large, R.R.; McGoldrick, P.J. The importance of oxidized brines for the formation of Australian Proterozoic stratiform sediment-hosted Pb–Zn (SEDEX) deposits. *Econ. Geol.* **2000**, *95*, 1–18. [CrossRef]
8. Large, R.R.; Bull, S.W.; McGoldrick, P.J.; Walters, S.; Derrick, G.M.; Carr, G.R. Stratiform and strata-bound Zn–Pb–Ag deposits in Proterozoic sedimentary basins, northern Australia. *Econ. Geol.* **2005**, *100*, 931–963.
9. Sangster, D.F. Evidence that Broken Hill-type Pb–Zn deposits are metamorphosed SEDEX deposits. *Miner. Deposita* **2020**, *55*, 1263–1270. [CrossRef]
10. Box, S.E.; Bookstrom, A.A.; Anderson, R.G. Origins of mineral deposits, Belt-Purcell basin, United States and Canada: An introduction. *Econ. Geol.* **2010**, *107*, 1081–1088. [CrossRef]
11. Newberry, R.J.; Einaudi, M.T.; Eastman, H.S. Zoning and genesis of the Darwin Pb–Zn–Ag skarn deposit, California: A reinterpretation based on new data. *Econ. Geol.* **1991**, *86*, 960–982. [CrossRef]
12. Roache, T.J.; Williams, P.J.; Richmond, J.M.; Chapman, L.H. Vein and skarn formation at the Cannington Ag–Pb–Zn deposit, Northeastern Australia. *Can. Mineral.* **2009**, *43*, 241–262. [CrossRef]
13. Megaw, P.K.; Ruiz, J.; Titley, S.R. High-temperature, carbonate-hosted Ag–Pb–Zn (Cu) deposits of northern Mexico. *Econ. Geol.* **1988**, *83*, 1856–1885. [CrossRef]
14. Yang, F.; Wu, G.; Li, R.H.; Zhang, T.; Chen, G.Z.; Xu, Y.M.; Li, Y.L.; Li, T.G.; Liu, R.H.; Chen, Y.J. Age, fluid inclusion, and H–O–S–Pb isotope geochemistry of the Baiyinchagan Sn–Ag–polymetallic deposit in the southern Great Xing'an Range, NE China. *Ore Geol. Rev.* **2022**, *150*, 105194. [CrossRef]
15. Ouyang, H.G.; Mao, J.W.; Santosh, M.; Zhou, J.; Zhou, Z.H.; Wu, Y.; Hou, L. Geodynamic setting of Mesozoic magmatism in NE China and surrounding regions: Perspectives from spatio–temporal distribution patterns of ore deposits. *J. Asian Earth Sci.* **2013**, *78*, 222–236. [CrossRef]
16. Camprubí, A.; Albinson, T. Epithermal deposits in México—Update of current knowledge, and an empirical reclassification. *Geol. Soc. Am. Spec. Pap.* **2007**, *422*, 377–415.
17. Wang, L.; Qin, K.Z.; Song, G.X.; Li, G.M. A review of intermediate sulfidation epithermal deposits and subclassification. *Ore Geol. Rev.* **2019**, *107*, 434–456. [CrossRef]
18. Zhai, D.G.; Williams-Jones, A.E.; Liu, J.J.; Selby, D.; Voudouris, P.C.; Tombros, S.; Li, K.; Li, P.L.; Sun, H.J. The genesis of the giant Shuangjianzishan epithermal Ag–Pb–Zn deposit, Inner Mongolia, northeastern China. *Econ. Geol.* **2020**, *115*, 101–128. [CrossRef]
19. Macario, P.R. Metallogenesis of the Penasquito Polymetallic Deposit: A Contribution to the Understanding of the Magmatic Ore System. Ph.D. Thesis, University of Nevada, Reno, NV, USA, 2016; pp. 1–310.
20. Wang, J.B.; Wang, Y.W.; Wang, L.J.; Uemoto, T. Tin–polymetallic mineralization in the southern part of the Da Hinggan Mountains, China. *Resour. Geol.* **2001**, *51*, 283–291. [CrossRef]
21. Zhou, Z.H.; Mao, J.W.; Lyckberg, P. Geochronology and isotopic geochemistry of the A-type granites from the Huanggang Sn–Fe deposit, southern Great Hinggan Range, NE China: Implication for their origin and tectonic setting. *J. Asian Earth Sci.* **2012**, *49*, 272–286. [CrossRef]
22. Ouyang, H.G.; Mao, J.W.; Zhou, Z.H.; Su, H.M. Late Mesozoic metallogeny and intracontinental magmatism, southern Great Xing'an Range, northeastern China. *Gondwana Res.* **2015**, *27*, 1153–1172. [CrossRef]
23. Liu, H.; Yuan, F.; Zhao, S.J.; Fan, M.J.; Guo, X.G. SHRIMP U–Pb Zircon Ages, Geochemistry and Sr–Nd–Hf Isotope Systematics of the Zalute Intrusive Suite in the Southern Great Xing'an Range, NE China: Petrogenesis and Geodynamical Implications. *Minerals* **2020**, *10*, 927. [CrossRef]
24. Mao, J.W.; Zhou, Z.H.; Wu, G.; Jiang, S.H.; Liu, C.L.; Li, H.M.; Ouyang, H.G.; Liu, J. Metallogenic regularity and minerogenetic series of ore deposits in Inner Mongolia and adjacent areas. *Miner. Depos.* **2013**, *32*, 715–729, (In Chinese with English Abstract).
25. Ouyang, H.G.; Mao, J.W.; Santosh, M.; Wu, Y.; Hou, L.; Wang, X.F. The Early Cretaceous Weilasituo Zn–Cu–Ag vein deposit in the southern Great Xing'an Range, northeast China: Fluid inclusions, H, O, S, Pb isotope geochemistry and genetic implications. *Ore Geol. Rev.* **2014**, *56*, 503–515. [CrossRef]

26. Li, S.H.; Li, Z.X.; Chen, G.Z.; Yi, H.N.; Yang, F.; Lü, X.; Shi, J.P.; Dou, H.B.; Wu, G. Age, Fluid Inclusion, and H–O–S–Pb Isotope Geochemistry of the Superlarge Huaaobaote Ag–Pb–Zn Deposit in the Southern Great Xing'an Range, NE China. *Minerals* **2023**, *13*, 939. [CrossRef]
27. Wu, G.; Liu, R.L.; Chen, G.Z.; Li, T.G.; Li, R.H.; Li, Y.L.; Yang, F.; Zhang, T. Mineralization of the Weilasituo rare metal–tin–polymetallic ore deposit in Inner Mongolia: Insights from fractional crystallization of granitic magmas. *Acta Petrol. Sin.* **2021**, *37*, 637–664. (In Chinese with English Abstract)
28. Wang, F.X.; Bagas, L.; Jiang, S.H.; Liu, Y.F. Geological, geochemical, and geochronological characteristics of Weilasituo Sn–polymetal deposit, Inner Mongolia, China. *Ore Geol. Rev.* **2017**, *80*, 1206–1229. [CrossRef]
29. Chen, G.Z.; Wu, G.; Li, T.G.; Liu, R.L.; Li, R.H.; Li, Y.L.; Yang, F. Mineralization of the Daolundaba Cu–Sn–W–Ag deposit in the southern Great Xing'an Range, China: Constraints from geochronology, geochemistry, and Hf isotope. *Ore Geol. Rev.* **2021**, *133*, 104–117. [CrossRef]
30. Chen, G.Z.; Wu, G.; Yang, F.; Zhang, T.; Li, T.G.; Liu, R.L.; Li, R.H.; Li, Y.L.; Wu, L.W.; Zhang, P.C. Ages, H–O–C–S–Pb isotopes, and fluid inclusion study of the Daolundaba Cu–Sn–W–Ag deposit in Inner Mongolia, NE China. *Ore Geol. Rev.* **2022**, *150*, 105171. [CrossRef]
31. Yang, F.; Wu, G.; Li, R.H.; Zhang, T.; Chen, G.Z.; Chen, Y.J. Petrogenesis of the Alubaogeshan intrusion in the Maodeng–Xiaogushan area, southern Great Xing'an Range, NE China: Implications for magma evolution and tin–polymetallic mineralization. *J. Asian Earth Sci.* **2022**, *238*, 105395. [CrossRef]
32. Yang, F.; Wu, G.; Chen, G.Z.; Li, S.H.; Li, Y.L.; Zhang, T.; Chen, Y.J. Petrogenesis and implications for tin mineralization of the Beidashan granitic pluton, southern Great Xing'an Range, NE China: Constraints from whole-rock and accessory mineral geochemistry. *J. Asian Earth Sci.* **2023**, *259*, 105883. [CrossRef]
33. Kuang, Y.S.; Zheng, G.R.; Lu, M.J.; Liu, Y.L.; Zhang, S.J.; Li, R.Y.; Cheng, W.J. Basic characteristics of Shuangjianzishan silver polymetallic deposit in Chifeng City, Inner Mongolia. *Miner. Depos.* **2014**, *33*, 847–856. (In Chinese with English Abstract)
34. Large, R.R.; Bull, S.W.; Selley, D.; Yang, J.W.; Cooke, D.R.; Garven, G.; McGoldrick, P.J. Controls on the Formation of Giant Stratiform Sediment-Hosted Zn–Pb–Ag Deposits: With Particular Reference to the North Australian Proterozoic. In *Giant Ore Deposits: Characteristics, Genesis and Exploration*; Centre for Special Ore Deposit and Exploration (CODES) Special Publication; Cooke, D.R., Pongratz, J., Eds.; University of Tasmania: Hobart, Australia, 2002; Volume 4, pp. 107–149.
35. Xu, Z.G.; Chen, Y.C.; Wang, D.H.; Chen, Z.H.; Li, H.M. *Scheme of the Classification of the Minerogenetic Units in China*; Geological Publishing House: Beijing, China, 2008; pp. 1–128. (In Chinese)
36. Hedenquist, J.W.; Lowenstern, J.B. The role of magmas in the formation of hydrothermal ore deposits. *Nature* **1994**, *370*, 519–527. [CrossRef]
37. Wang, F.X.; Bagas, L.; Jiang, S.H.; Zhang, F.X.; Liu, Y.F.; Chong, X.X. Geochronology and ore genesis of the Shuangjianzishan Ag–polymetallic deposit, Inner Mongolia, China. *Ore Geol. Rev.* **2019**, *107*, 1020–1045. [CrossRef]
38. Liu, C.H.; Leon, B.; Wang, F.X. Isotopic analysis of the superlarge Shuangjianzishan Pb–Zn–Ag deposit in Inner Mongolia, China: Constraints on magmatism, metallogenesis, and tectonic setting. *Ore Geol. Rev.* **2016**, *75*, 252–267. [CrossRef]
39. Wu, G.B.; Liu, J.M.; Zeng, Q.D.; Sun, H.S.; Liu, M.T. The metallogenic age of Shuangjianzishan Ag–Pb–Zn deposit of Great Hinggan Range, Inner Mongolia. *Acta Miner. Sin.* **2013**, *33*, 619. (In Chinese with English Abstract)
40. Zhang, H.Y.; Zhai, D.G.; Liu, J.J.; Li, P.L.; Li, K.; Sun, H.J. Fluid inclusion and stable (H–O–C) isotope studies of the giant Shuangjianzishan epithermal Ag–Pb–Zn deposit, Inner Mongolia, NE China. *Ore Geol. Rev.* **2019**, *115*, 103–170. [CrossRef]
41. Xue, J.X.; Shi, Y.; Liu, Z.H.; Xue, L.F. Closure of the Eastern Paleo-Asian Ocean: Evidence from Permian–Triassic Volcanic Rocks in the Northern Margin of the North China Craton. *Minerals* **2023**, *13*, 606. [CrossRef]
42. Wang, T.; Guo, L.; Zheng, Y.D.; Donskaya, T.; Gladkochub, D.; Zeng, L.S.; Li, J.B.; Wang, Y.B.; Mazukabzov, A. Timing and processes of late Mesozoic mid–lower-crustal extension in continental NE Asia and implications for the tectonic setting of the destruction of the North China Craton: Mainly constrained by zircon U–Pb ages from metamorphic core complexes. *Lithos* **2012**, *154*, 315–345. [CrossRef]
43. Chen, B.; Jahn, B.M.; Tian, W. Evolution of the Solonker suture zone: Constraints from zircon U–Pb ages, Hf isotopic ratios and whole-rock Sr–Nd isotope compositions of subduction- and collision-related magmas and forearc sediments. *J. Asian Earth Sci.* **2009**, *34*, 245–257. [CrossRef]
44. Lu, L.; Qin, Y.; Zhang, K.J.; Han, C.Y.; Wei, T.; Li, F.Z.; Qu, Z.H. Provenance and tectonic settings of the late Paleozoic sandstones in central Inner Mongolia, NE China: Constraints on the evolution of the southeastern Central Asian Orogenic Belt. *Gondwana Res.* **2019**, *77*, 111–135. [CrossRef]
45. Xu, W.L.; Pei, F.P.; Wang, F.; Meng, E.; Ji, W.Q.; Yang, D.B.; Wang, W. Spatialtemporal relationships of Mesozoic volcanic rocks in NE China: Constraints on tectonic overprinting and transformations between multiple tectonic regimes. *J. Asian Earth Sci.* **2013**, *74*, 167–193. [CrossRef]
46. Zhou, J.B.; Li, L. The Mesozoic accretionary complex in Northeast China: Evidence for the accretion history of Paleo-Pacific subduction. *J. Asian Earth Sci.* **2017**, *145*, 91–100. [CrossRef]
47. Dong, P.P.; Li, Y.J.; Xie, Y.; Wang, J.F.; Li, H.Y. Petrogenesis of the Late Carboniferous Trondhjemite in Central Inner Mongolia in North China and Constraints of Intra-Oceanic Subduction in the Southern Paleo-Asian Ocean. *Minerals* **2022**, *12*, 1212. [CrossRef]

48. Zhang, J.H.; Gao, S.; Ge, W.C.; Wu, F.Y.; Yang, J.H.; Wilde, S.A.; Li, M. Geochronology of the Mesozoic volcanic rocks in the Great Xing'an Range, northeastern China: Implications for subduction-induced delamination. *Chem. Geol.* **2010**, *276*, 144–165. [CrossRef]
49. Zhai, D.G.; Liu, J.J.; Zhang, H.Y.; Tombros, S.; Zhang, A.L. A magmatic-hydrothermal origin for Ag–Pb–Zn vein formation at the Bianjiadayuan deposit, Inner Mongolia, NE China: Evidences from fluid inclusion, stable (C–H–O) and noble gas isotope studies. *Ore Geol. Rev.* **2018**, *101*, 1–16. [CrossRef]
50. Griffin, W.L.; Belousova, E.A.; Shee, S.R.; Pearson, N.J.; O'reilly, S.Y. Archean crustal evolution in the northern Yilgarn Craton: U–Pb and Hf-isotope evidence from detrital zircons. *Precambrian Res.* **2004**, *131*, 231–282. [CrossRef]
51. Frei, D.; Gerdes, A. Precise and accurate in situ U–Pb dating of zircon with high sample throughput by automated LA–SF–ICP–MS. *Chem. Geol.* **2009**, *261*, 261–270. [CrossRef]
52. Jackson, S.E.; Pearson, N.J.; Griffin, W.L.; Belousova, E.A. The application of laser ablation-inductively coupled plasma-mass spectrometry to in situ U–Pb zircon geochronology. *Chem. Geol.* **2004**, *211*, 47–69. [CrossRef]
53. Black, L.P.; Gulson, B.L. The age of the mud tank carbonatite, strangways range, northern territory. *Geol. Geophys.* **1978**, *3*, 227–232.
54. Ludwig, K.R. *User's Manual for Isoplot/Ex, Version 3.0, A Geochronological Toolkit for Microsoft Excel*; Berkeley Geochronology Center: Berkeley, CA, USA, 2003; pp. 1–74.
55. Andersen, T. Correction of common lead in U–Pb analyses that do not report $^{204}$Pb. *Chem. Geol.* **2002**, *192*, 59–79. [CrossRef]
56. Bodnar, R.J. Revised equation and table for determining the freezing-point depression of $H_2O$–NaCl solutions. *Geochim. Cosmochim. Acta* **1993**, *57*, 683–684. [CrossRef]
57. Brown, P.E. FLINCOR: A microcomputer program for the reduction and investigation of fluid-inclusion data. *Am. Mineral.* **1989**, *74*, 1390–1393.
58. Clayton, R.N.; Mayeda, T.K. The use of bromine pentafluoride in the extraction of oxygen from oxides and silicates for isotopic analysis. *Geochim. Cosmochim. Acta* **1963**, *27*, 43–52. [CrossRef]
59. Coleman, M.L.; Shepherd, T.J.; Durham, J.J.; Rouse, J.E.; Moore, G.R. Reduction of water with zinc for hydrogen isotope analysis. *Anal. Chem.* **1982**, *54*, 993–995. [CrossRef]
60. Clayton, R.N.; Mayeda, T.K.; Oneil, J.R. Oxygen isotope: Exchange between quartz and water. *J. Geophys. Res.-Earth* **1972**, *77*, 3057–3067. [CrossRef]
61. Todt, W.; Cliff, R.A.; Hanser, A.; Hofmann, A.W. Re-calibration of NBS lead standards using a $^{202}$Pb–$^{205}$Pb double spike. *Terra Abstr.* **1993**, *5*, 396.
62. Goldstein, R.H.; Reynolds, T.J. *Systematics of Fluid Inclusions in Diagenetic Minerals*; SEPM Society for Sedimentary Geology: Tulsa, OK, USA, 1994; pp. 1–199.
63. Sheppard, S.M.F. Characterization and isotopic variations in natural-waters. *Rev. Mineral. Geochem.* **1986**, *16*, 165–183.
64. Chen, Y.W.; Mao, C.X.; Zhu, B.Q. Lead isotopic composition and genesis of Phanerozoic metal deposit in China. *Geochemistry* **1982**, *1*, 137–158. [CrossRef]
65. Cui, M. The Geochemical Characteristics and Diagenesis of Ore-Forming Diorite-Porphyrite from Shuangjianzishan Ag Polymetallic Deposit in Inner Mongolia. Master's Thesis, China University of Geosciences (Beijing), Beijing, China, 2015. (In Chinese with English Abstract).
66. Ouyang, H.G.; Li, R.H.; Zhou, Z.H. The Jurassic mineralization of the Shuangjianzishan Ag-polymetallic deposit and its significance in prospecting: Evidence from geochronology. *Acta Geol. Sin.* **2016**, *90*, 1835–1845, (In Chinese with English Abstract).
67. Wang, F.X. Magmatic Activity and Silver Polymetallic Mineralization in the Shuangjianzishan Silver Polymetallic Deposit and Its Surrounding Areas in Inner Mongolia. Ph.D. Thesis, China University of Geosciences, Wuhan, China, 2018; pp. 1–189. (In Chinese with English Abstract)
68. Wu, Y.H.; Han, J.T.; Liu, Y.H.; Ma, G.Q.; Han, F.X.; Yang, Y.C.; Liu, L.J.; Guo, L.; Guan, Y.; Zhang, Y.H.; et al. Metallogenic model of the Shuangjianzishan Ag–Pb–Zn district, Northeast China: Revealed from integrated geophysical investigation. *Geosci. Front.* **2022**, *13*, 101321. [CrossRef]
69. Wang, F.X.; Sun, H.J.; Pei, R.F.; Liu, Y.F.; Liu, C.H.; Jiang, S.H. The geologic features and genesis of Shuangjianzishan silver–polymetallic deposit, Balinzuo Qi, Inner Mongolia. *Geol. Rev.* **2016**, *62*, 1241–1256. (In Chinese with English Abstract)
70. Liu, Y.F.; Jiang, S.H.; Bagas, L. The genesis of metal zonation in the Weilasituo and Bairendaba Ag–Zn–Pb–Cu–(Sn–W) deposits in the shallow part of a porphyry Sn–W–Rb system, Inner Mongolia, China. *Ore Geol. Rev.* **2016**, *75*, 150–173. [CrossRef]
71. Yang, F.; Sun, J.G.; Wang, Y.; Fu, J.Y.; Na, F.C.; Fan, Z.Y.; Hu, Z.Z. Geology, Geochronology and Geochemistry of Weilasituo Sn-Polymetallic Deposit in Inner Mongolia, China. *Minerals* **2019**, *9*, 104. [CrossRef]
72. Rye, R.O.; Ohmoto, H. Sulfur and carbon isotopes and ore genesis: A review. *Econ. Geol.* **1974**, *69*, 826–842. [CrossRef]
73. Wilkinson, J.J.; Jenkin, G.R.T.; Fallick, A.E.; Foster, R.P. Oxygen and hydrogen isotopic evolution of Variscan crustal fluids, south Cornwall, UK. *Chem. Geol.* **1995**, *123*, 239–254. [CrossRef]
74. Ohmoto, H. Formation of volcanogenic massive sulfide deposits: The Kuroko perspective. *Ore Geol. Rev.* **1996**, *10*, 135–177. [CrossRef]
75. Taylor, H.P., Jr.; Frechen, J.; Degens, E.T. Oxygen and carbon isotope studies of carbonatites from the Laacher See District, West Germany and the Alnö District, Sweden. *Geochim. Cosmochim. Acta* **1967**, *31*, 407–430. [CrossRef]
76. Hoefs, J. Isotope Fractionation Processes of Selected Elements. In *Stable Isotope Geochemistry*, 9th ed.; Springer Nature Switzerland AG: Cham, Switzerland, 2021; pp. 1–528.

77. Faure, G. *Origin of Igneous Rocks: The Isotopic Evidence*; Springer Science & Business Media: Cham, Switzerland, 2013; pp. 1–398.
78. Townley, B.K.; Godwin, C.I. Isotope characterization of lead in galena from ore deposits of the Aysen Region, southern Chile. *Miner. Depos.* **2001**, *36*, 45–57. [CrossRef]
79. Kamenov, G.D.; Macfarlane, A.W.; Riciputi, L.R. Sources of lead in the San Cristobal, Pulacayo, and Potosi mining districts, Bolivia, and a revaluation of regional ore lead isotope provinces. *Econ. Geol.* **2002**, *97*, 573–592.
80. Marcoux, E.; Grancea, I.; Lupulescu, M. Lead isotope signatures of epithermal and porphyry-type ore deposits from the Romanian Carpathian Mountains. *Miner. Depos.* **2002**, *37*, 173–184. [CrossRef]
81. Chiaradia, M.; Fontboté, L.; Paladines, A. Metal sources in mineral deposits and crustal rocks of Ecuador (1 N–4 S): A lead isotope synthesis. *Econo. Geol.* **2004**, *99*, 1085–1106.
82. Zartman, R.E.; Doe, B.R. Plumbotectonics: The model. *Tectonophysics* **1981**, *75*, 135–162. [CrossRef]
83. Zhu, B.Q. Tri-dimension spacial topological diagrams of ore lead isotopes and their application to the division of geochemical provinces and mineralizations. *Geochimica* **1993**, *21*, 209–216. (In Chinese with English Abstract)
84. Richards, J.P. Magmatic to hydrothermal metal fluxes in convergent and collided margins. *Ore Geol. Rev.* **2011**, *40*, 1–26. [CrossRef]
85. Pearson, R.G. Hard and soft acids and their bases. *J. Am. Chem. Soc.* **1963**, *85*, 3533–3539. [CrossRef]
86. Stefansson, A.; Seward, T.M. Experimental determination of the stability and stoichiometry of sulphide complexes of silver (I) in hydrothermal solutions to 400 degrees. *Geochim. Cosmochim. Acta* **2003**, *67*, 1395–1413. [CrossRef]
87. Williams-Jones, A.E.; Migdisov, A.A. Experimental Constraints on the Transport and Deposition of Metals in Ore-Forming Hydrothermal Systems. In *Building Exploration Capability for the 21st Century*; Society of Economic Geologists, Inc.: Littleton, CO, USA, 2014; pp. 77–95.
88. Zhong, R.C.; Brugger, J.; Chen, Y.J.; Li, W.B. Contrasting regimes of Cu, Zn and Pb transport in ore-forming hydrothermal fluids. *Chem. Geol.* **2015**, *395*, 154–164. [CrossRef]
89. Wood, S.A.; Samson, I.M. The hydrothermal geochemistry of tungsten in granitoid environments: I. Relative solubilities of ferberite and scheelite as a function of T, P, pH, and m (NaCl). *Econ. Geol.* **2000**, *95*, 143–182. [CrossRef]
90. Pirajno, F. *Hydrothermal Processes and Mineral Systems*; Springer Science & Business Media B.V.: Perth, Australia, 2009; pp. 1–1250.
91. Seward, T.M.; Williams-Jones, A.E.; Migdisov, A.A. The Chemistry of Metal Transport and Deposition by Ore-Forming Hydrothermal Fluids. In *Treatise on Geochemistry*; Elsevier Ltd.: Amsterdam, The Netherlands, 2014; pp. 29–57.
92. Korges, M.; Weis, P.; Lüders, V.; Laurent, O. Depressurization and boiling of a single magmatic fluid as a mechanism for tin–tungsten deposit formation. *Geology* **2017**, *46*, 75–78. [CrossRef]
93. Jiang, S.H.; Chen, C.L.; Bagas, L.; Liu, Y.; Han, N.; Kang, H.; Wang, Z.H. Two mineralization events in the Baiyinnuoer Zn–Pb deposit in Inner Mongolia, China: Evidence from field observations, S–Pb isotopic compositions and U–Pb zircon ages. *J. Asian Earth Sci.* **2017**, *144*, 339–367. [CrossRef]
94. Zhao, J.Q.; Zhou, Z.H.; Ouyang, H.G.; Chen, B.Q.; Liu, W.J.; Yang, F. Zircon U–Pb age and geochemistry of quartz syenite porphyry in Shuangjianzishan Ag–Pb–Zn (Sn) deposit, Inner Mongolia, and their geological implications. *Miner. Depos.* **2022**, *41*, 324–344, (In Chinese with English Abstract).
95. Chinchilla, D.; Ortega, L.; Piña, R.; Merinero, R.; Moncada, D.; Bodnar, R.J.; Quesada, C.; Valverde, C.; Lunar, R. The Patricia Zn–Pb–Ag epithermal ore deposit: An uncommon type of mineralization in northeastern Chile. *Ore Geol. Rev.* **2016**, *73*, 104–126. [CrossRef]
96. Sillitoe, R.H. Porphyry copper systems. *Econ. Geol.* **2010**, *105*, 3–41. [CrossRef]